PCCP

PAPER

View Article Online
View Journal | View Issue

Check for updates

Cite this: *Phys. Chem. Chem. Phys.*, 2021, **23**, 23886

Critical role of H-aggregation for high-efficiency photoinduced charge generation in pristine pentamethine cyanine salts†

George C. Fish,[a] Juan Manuel Moreno-Naranjo,‡[a] Andreas Billion,[b] Daniel Kratzert,[b] Erwin Hack,[c] Ingo Krossing,[b] Frank Nüesch[de] and Jacques-E. Moser*[a]

Received 16th July 2021,
Accepted 8th October 2021

DOI: 10.1039/d1cp03251h

rsc.li/pccp

The mechanism of photoinduced symmetry-breaking charge separation in solid cyanine salts at the base of organic photovoltaic and optoelectronic devices is still debated. Here, we employ femtosecond transient absorption spectroscopy (TAS) to monitor the charge transfer processes occurring in thin films of pristine pentamethine cyanine (Cy5). Oxidized dye species are observed in Cy5-hexafluorophosphate salts upon photoexcitation, resulting from electron transfer from monomer excited states to H-aggregates. The charge separation proceeds with a quantum yield of 86%, providing the first direct proof of high efficiency intrinsic charge generation in organic salt semiconductors. The impact of the size of weakly coordinating anions on charge separation and transport is studied using TAS alongside electroabsorption spectroscopy and time-of-flight techniques. The degree of H-aggregation decreases with increasing anion size, resulting in reduced charge transfer. However, there is little change in carrier mobility, as despite the interchromophore distance increasing, the decrease in energetic disorder helps to alleviate the trapping of charges by H-aggregates.

Introduction

Cyanine dyes, and their derivatives, have a long history in the field of small molecule-based organic photovoltaics (OPV).[1] The beneficial properties of cyanine dyes, such as their high extinction coefficients (typically exceeding 10^5 L mol^{-1} cm^{-1})[2] mean that they have traditionally been used in planar architecture devices, generally in combination with fullerene acceptor materials, with device efficiencies of up to 3.7% being achieved.[3] Their aforementioned high extinction coefficients mean that thin active layers, of around 20 nm thickness, can be employed allowing them to circumvent issues that typically thwart the performance of planar architecture devices, such as exciton recombination before diffusion to the donor acceptor interface has occurred.[4,5]

The cyanine dyes used in the OPV field comprise of a positively charged chromophore paired with a counterion; the chromophore generally consists of two heterocycles connected with a polymethine chain, the length of which can be altered to change the absorption profile of the dye. This has led to new applications for these dyes, such as in transparent devices, due to their high absorption in the near infrared and high transparency in the visible.[6,7]

Furthermore, the counterion can also be easily changed using ion exchange techniques,[8] which allows for a wide variety of counterions to be employed including weakly coordinating anions (WCAs).[9] While it is not possible for anions to be non-coordinating, WCAs closely approximate non-coordinating conditions[10,11] and allow for preparation of ionic liquids virtually without ion pairing.[12,13] Changing the counterion impacts upon the thin film properties as well as the device performance.[14,15]

Previous work regarding ultrafast processes in cyanine dyes has tended to focus on the fundamental photophysics of the cyanine chromophore in solution, such as the triplet state

[a] *Photochemical Dynamics Group, Institute of Chemical Sciences and Engineering, École polytechnique fédérale de Lausanne, Station 6, 1015 Lausanne, Switzerland. E-mail: je.moser@epfl.ch*
[b] *Institut für Anorganische und Analytische Chemie, and Freiburger Materialforschungszentrum, Universität Freiburg, Albertstrasse 21, 79104 Freiburg, Germany*
[c] *Laboratory for Transport at Nanoscale Interfaces, Swiss Federal Laboratories for Materials Science and Technology, Empa, Überlandstrasse 129, 8600 Dübendorf, Switzerland*
[d] *Laboratory for Functional Polymers, Swiss Federal Laboratories for Materials Science and Technology, Empa, Überlandstrasse 129, 8600 Dübendorf, Switzerland*
[e] *Institute of Materials, School of Engineering, École polytechnique fédérale de Lausanne, Station 12, 1015 Lausanne, Switzerland*

† Electronic supplementary information (ESI) available. See DOI: 10.1039/d1cp03251h

‡ Current address: Department of Chemistry, Molecular Sciences Research Hub, Imperial College London, White City Campus, London, W12 OBZ, UK.

This journal is © the Owner Societies 2021

characteristics[16] and the dynamics of higher lying excited states.[17] The majority of studies pertaining to ultrafast processes in cyanine based OPVs have focused on cyanine:C_{60} bilayers. For example, time-resolved electroabsorption spectroscopy has been used to study the dissociation of charge transfer states in Cy3-P:C_{60} bilayers.[18] Moving away from bilayers, transient absorption spectroscopy has been employed to study the impact of phase morphology in cyanine:PCBM blends, providing a better understanding of charge transfer dynamics in bulk heterojunction architecture OPVs.[19] More recently, evidence was produced demonstrating that photocurrent generation can occur in a pristine cyanine thin film, despite the absence of a donor–acceptor interface.[20] Furthermore, the generated charges exhibited a long carrier lifetime as a result of reduced recombination, providing potential material design concepts for future photodiodes. Cyanines have been utilised in several different photodiode designs, being employed to take advantage of their narrow band absorption, potential for high absorption in the near infrared,[21] and ability to form J-aggregates.[22–25]

Intrinsic photogeneration has also been previously demonstrated in photodiodes utilising donor–acceptor oligomers,[26] as well as in single layer SubNc, SubPc and squaraine dye-based devices. Here, the intrinsic charge generation was attributed to the high dielectric constant, resulting in efficient screening and therefore allowing free carrier generation.[27,28] In comparison, cyanine dye-based photodiodes have shown substantially higher photon-to-electron quantum yields[20] and could be a suitable and versatile alternative material to use in single layer photodiodes. The understanding of the symmetry-breaking charge separation mechanism, however, is still lacking and would spur the development of new materials design.

In this work, ultrafast transient absorption spectroscopy was used to unravel the photoinduced charge transfer mechanism in pristine pentamethine cyanine dyes, providing the first direct proof of high efficiency intrinsic charge generation in organic salt semiconductors. Furthermore, the impact of the counterion on the charge transfer process was assessed using four different counterions of varying sizes; the purpose of this was to vary the degree of interaction between the cyanine chromophores in the different dyes, and thus study its effect on the photogeneration of charges.

Finally, electroabsorption spectroscopy and time-of-flight (TOF) were used to determine the impact of counterion size on charge transport within the solid dye film.

Experimental section

Sample preparation

The cyanine dyes 2-[3-(1,3-dihydro-1,3,3-trimethyl-2*H*-indol-2-ylidene)-propenyl]-1,3,3-trimethyl-3*H*-indolium chloride (Cy5-Cl) and its hexafluorophosphate analogue (Cy5-P) were purchased from FEW Chemicals, Germany. The tetrakis(nonafluoro-*tert*-butoxy)aluminate ($Al(pftb_4)$) and tetrakis(perfluoro-1-adamantoxy)aluminate ($Al(pfad)_4$) WCA Cy5 salts were provided by the group of Prof. Ingo Krossing, and their synthesis is described in the ESI,† (S1).

The Cy5-Cl and Cy5-P dyes were dissolved in acetonitrile (Sigma Aldrich), while the two Al WCA salts were dissolved in ethanol (Sigma Aldrich) in various concentrations. Thin films were subsequently fabricated by spin coating the solutions onto cleaned glass substrates inside a glovebox. All chemicals were used as supplied without further purification.

Samples for electroabsorption (EA) and time-resolved electroabsorption spectroscopy (TREAS) were prepared on glass patterned with fluorine-doped tin oxide (FTO). Spin coating aluminium sec-butoxide (0.25 M) in 2-methoxyethanol, calcination at 500 °C for 1 hour, and repeating 3 times yielded the 20 nm aluminium oxide insulating layer. The cyanine dye was then deposited as mentioned above, followed by thermal deposition of an aluminium top electrode.

Samples for TOF were also prepared on substrates with 6 layers of alumina atop the FTO patterned glass. The cyanine dyes were deposited *via* spin coating at 6000 rpm for 60 s.

Thin film thickness and the optical constants were determined using both ellipsometry (J. A. Woollam M2000-VI) and cross-sectional SEM (Zeiss Merlin).

Spectroscopy

Absorption spectra were measured using a PerkinElmer Lambda 950 UV/vis/NIR spectrophotometer. Emission spectra were measured using a Horiba Jobin-Yvon Fluorolog-3 instrument with a photomultiplier tube as a detector.

Transient absorption (TA) spectra and electroabsorption (EA) spectra were measured using a femtosecond pump–probe spectrometer based on an amplified Ti:sapphire laser (Clark-MXR, CPA-2001) delivering 778 nm pulses of 150 fs at a 1 kHz repetition rate. In both cases, the pump beam was generated by passing a portion of the fundamental through a two-stage non-collinear optical parametric amplifier (NOPA-Plus, Clark-MXR) resulting in an excitation wavelength of 580 nm. The probe beam was constituted by a broadband white light continuum generated by passing part of the fundamental through a 5 mm-thick oscillating CaF_2 plate (for TA, 450–1050 nm), or through a 4 mm sapphire window (for EA, 400–750 nm). The pump and probe beams, set at magic angle polarization, were spatially and temporally overlapped with respect to one another using a delay stage. For TA measurements, samples were measured in transmission mode while EA measurements were measured in reflection mode. The probe beam was split into a signal beam passing through the sample and a reference passing next to it in order to account for shot-to-shot fluctuations. The signal and reference beams were dispersed in two respective grating spectrographs (SpectraPro 2500i, Princeton Instruments or SR163, Andor Instruments) and detected shot-to-shot at 1 kHz by 512 × 58 pixel back-thinned charge-coupled device cameras (Hamamatsu S07030-0906). For TA measurements, a chopper set at 500 Hz modulated the frequency of the pump beam enabling for the absorption with and without the pump to be acquired. For EA spectroscopy, the electric field across the sample was modulated at half the amplifier frequency (500 Hz),

BY-NC

using square pulses generated by a function generator (Tektronix AFG 2021, from −10 to 10 V, 100 μs pulse duration). The current responses across the samples were recorded using a 50 Ω series load with a 400 MHz bandpass oscilloscope (Tektronix TDS 3044B).

Time-of-flight

The excitation source was provided by a Nd:YAG Q-switched laser (Continuum Powerlite-7030) with a frequency-tripled output (355 nm) and a repetition rate of 0.2–20 Hz. This UV output was used to pump a broadband optical parametric oscillator (OPO-355, GWU) allowing for the wavelength of the excitation pulses (7 ns duration) to be tuned. A 24 V series battery was used to apply a voltage across the sample, and the samples only experienced a voltage during the single shot measurement. 10 shots were acquired to minimise the impact of oscillations, and between each measurement the voltage was switched off allowing the carriers to return to equilibrium. The photocurrent response from the samples was recorded using an oscilloscope (DPO 7104, Tektronix, 1 MΩ). A capacitor and a variable resistor box were placed in parallel to the battery in order to adjust the RC constant of the circuit.

Results and discussion

Femtosecond pump–probe transient absorption (TA) spectroscopy measurements were first carried out on a solution and thin film sample of 1,3,3-trimethyl-2-[5-(1,3,3-trimethyl-1,3-dihydro-indol-2-ylidene)-penta-1,3-dienyl]-3*H*-indolium hexafluorophosphate, which will from now on be referred to as Cy5-P. The structure of the Cy5 chromophore can be seen in Fig. 1a and the normalized absorption spectra for the solution and thin film are shown in Fig. 1b. The sharp peak at around 640 nm in the solution spectrum corresponds to the Cy5 monomer (0, 0) transition, while the shoulder peaks at wavelengths ≤600 nm are assigned to vibronic transitions. The thin-film absorption spectrum is red shifted, as expected, due to increased intermolecular interactions in the solid state and is broadened with two main features appearing at 620 and 680 nm, respectively. The latter of these two features corresponds to the Cy5 monomer, while the former is assigned to the absorption of the H-dimer.[29]

Furthermore, the H-dimer peak exhibits broadening in the blue region due to higher order H-aggregates. The thin film spectrum corresponds largely to the absorption coefficient measured by ellipsometry (ESI,† Fig. S4.2) meaning that

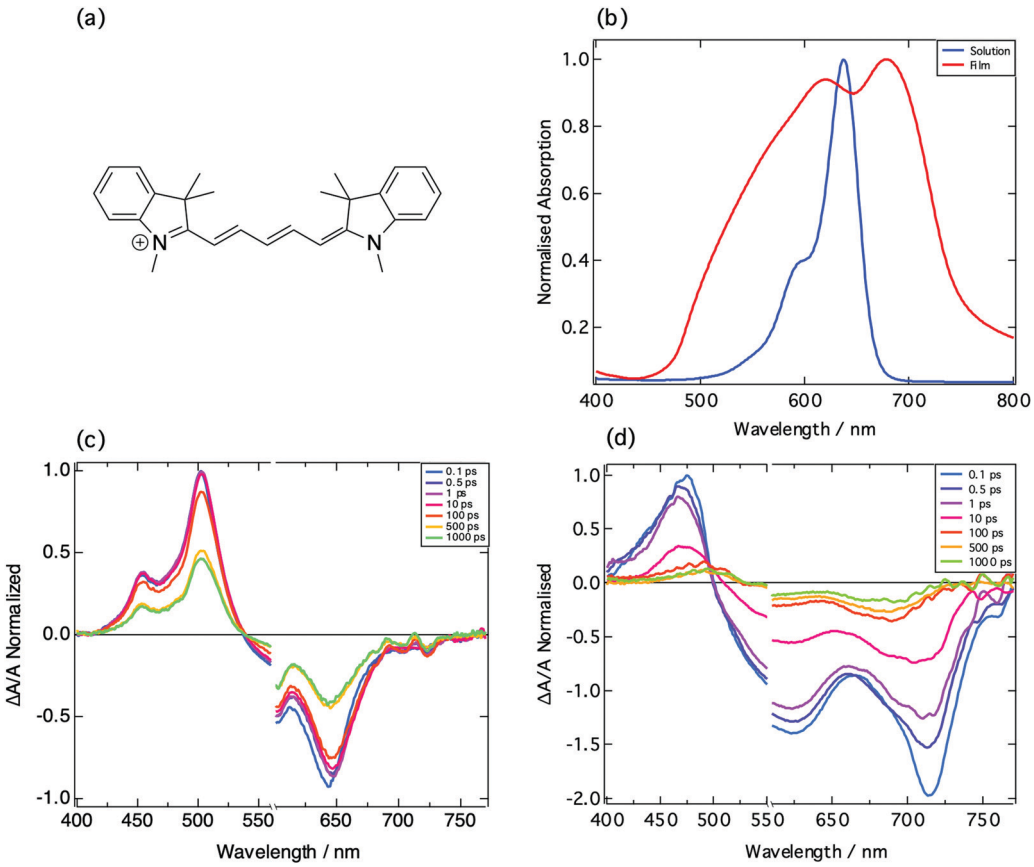

Fig. 1 (a) Structure of the Cy5 chromophore. (b) Absorption spectra of Cy5-P in acetonitrile and as a thin film. Normalized transient absorption spectra of Cy5-P solution (c) and thin film (d). Samples were excited at 580 nm. The transient absorption spectra were normalized to the 100 fs signal, and normalization was done for ease of comparison.

CC BY-NC

 This journal is © the Owner Societies 2021

reflectance and interference features are only minor contributions to the absorbance spectrum.

Pulsed laser excitation at 580 nm yielded the transient absorption spectra of the solution and thin-film of Cy5-P (Fig. 1c and d). Four main features can be seen in the TA spectrum of the solution: two positive features at 450 and 500 nm, along with two negative features at 540–615 and 650 nm. The two positive peaks arise from the same process, as they display the same time dependence. They also exhibit no fluence (see ESI,† Fig. S2.1) or concentration dependence, and so can be assigned to S_1–S_n transitions. Furthermore, this excited state absorption feature (ESA) is similar to those that have been seen previously.[30] It is expected that a second positive feature, corresponding to *trans–cis* photoisomerization, would be seen if a longer time window were monitored.[16] The negative band between 540 and 615 nm is assigned to ground state bleaching (GSB), due to its resemblance to the absorption spectrum of the monomer in the ground state. Finally, the negative feature at 650 nm corresponds to stimulated emission.

In comparison, the transient absorption spectrum for the Cy5-P film consists of three main features, of which the two negative features correspond to the GSB (620 nm) of the H-dimer and combined GSB and stimulated emission (680–720 nm). The major difference, however, between the solution and the film is the positive feature; unlike in the solution spectrum, the transient absorption spectrum of the film exhibits only a positive feature, which shifts towards higher wavelengths over time (from 470 nm at 0.1 ps to 495 nm at 1000 ps). The kinetics of this feature are also different to that of the ESA feature in the solution. Given that the proposed model for intrinsic charge generation in Cy5-P relies upon the generation of redox species,[20] it was postulated that the single positive feature in the transient absorption spectrum could arise from the absorption of the oxidized Cy5 chromophore.

To confirm this, bromine vapor was used to oxidize a Cy5-P film *in situ* and the absorption spectrum was subsequently measured. As seen in Fig. 2a, there are two processes which take place when the film is exposed to bromine vapor. The first process is the disruption of H-aggregates within the film. This is evident from the broadened shoulder which is present in the spectrum of the neat film, but absent upon exposure to the bromine vapor. The broadened shoulder corresponds to higher order H-aggregates and so its absence points towards the oxidation of these large aggregates within the film. This process appears to occur more quickly since a single oxidation step is able to extinguish a large aggregate composed of several chromophores.

The second process that takes place is then the oxidation of the cyanine chromophore in its monomeric state. Oxidation of the aggregated film, however, does not reveal the distinct peak at 470 nm seen in the transient absorption spectrum of Fig. 1d. A different behaviour is obtained when the chromophores are first oxidized in solution using $NOBF_4$. Here, the oxidized film shows precisely the expected feature with a peak at 470 nm (Fig. 2b). After de-doping in air for several hours, the

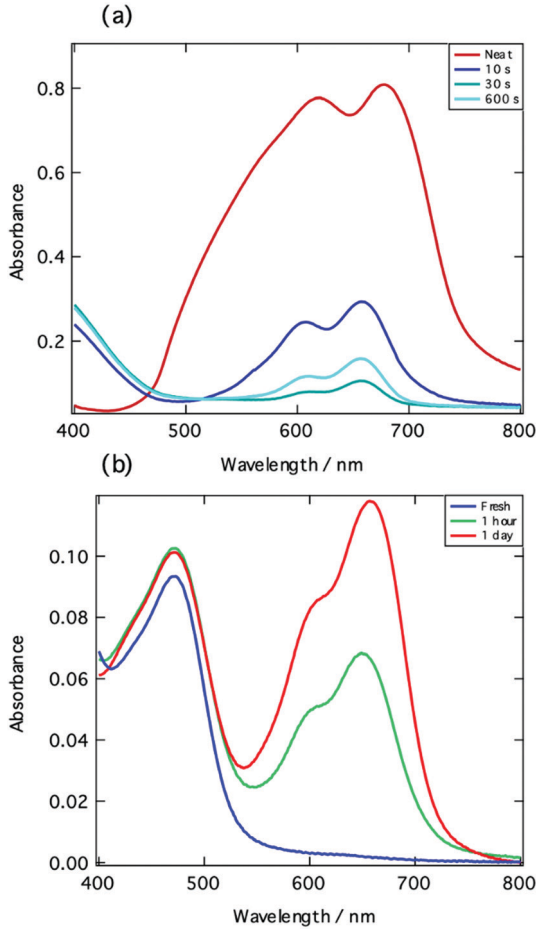

Fig. 2 (a) Absorption spectra of a thin film of Cy5-P before (red) and after (blue lines) exposure to bromine vapor for different amounts of time. (b) Absorption spectra of a thin film of Cy5-P : $NOBF_4$ 1 : 2.5 mol/mol blend ratio at different times after spin-coating.

monomer spectrum reappears. Since the film was cast from a Cy5-P : $NOBF_4$ 1 : 2.5 mol/mol solution in acetonitrile, the large amount of salt probably inhibits H-aggregate formation. Also, from an electrostatic point of view, the cyanine di-cations are not likely to stack in close packed H-stacks.

Due to the close match of the absorption features measured in the transient absorption spectrum and the film oxidized with $NOBF_4$, we are tempted to assign this positive feature to oxidized monomer species ($Cy5^+$) present in the Cy5-P film.

At this stage, we cannot completely exclude the possibility that the feature at 470 nm arises from the absorption of reduced species of Cy5 ($Cy5^-$), since absorption studies on electrochemically reduced pentamethine cyanine dyes revealed similar spectra for the neutral and the dicationic radicals.[31] Also, neutral cyanine radicals are very unstable, promptly undergoing dimerization and are therefore inaccessible in steady state measurements.

Having established the presence of oxidized or reduced cyanine chromophores within the photoexcited film, the impact of the interchromophore distance upon the charge generation process was investigated. Poly(methylmethacrylate), PMMA, was

CC BY-NC

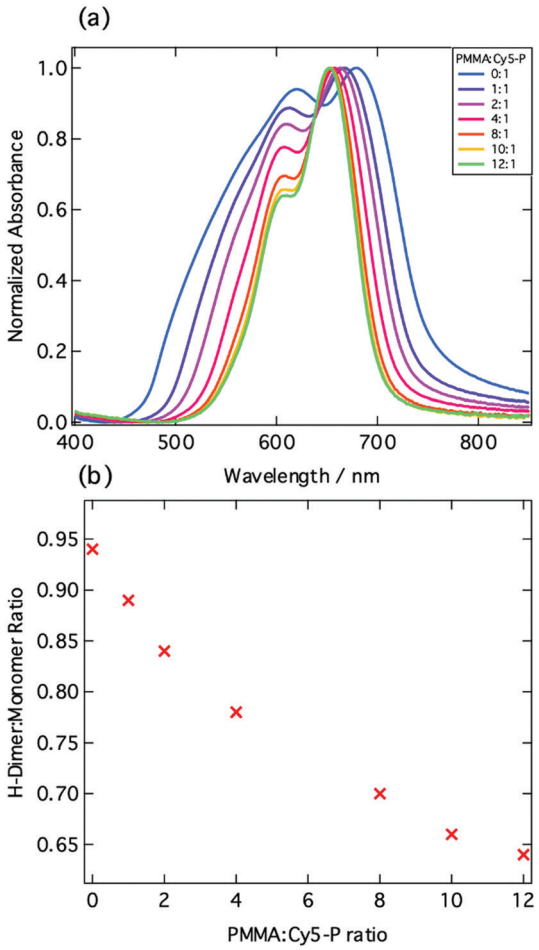

Fig. 3 (a) Normalized absorption spectra of varying ratios of PMMA : Cy5-P. (b) Ratio of H-dimer : monomer peak height as a function of the PMMA : Cy5-P blend ratio.

added to Cy5-P in various molar ratios and thin films were fabricated. From ground state absorption measurements, it is evident that as the proportion of PMMA increases there is a decrease in the degree of aggregation, which is evidenced by the decrease in the H-dimer peak height (Fig. 3a and b). We also note that there is a decrease in the FWHM as the PMMA : Cy5-P ratio increases. While the precise composition of the film including monomers, H-dimers, larger H-aggregates, and perhaps J-aggregates, is very difficult to determine, the FWHM provides a useful indicator. From Fig. 3a, we see that a FWHM value of 90 nm is reached for well separated monomer species.

From the TA spectra (Fig. 4a), it is evident that as the proportion of PMMA increases, resulting in the aforementioned decrease in aggregation, the positive feature transforms from one to two peaks which corresponds to the singlet excited state absorption as observed in solution (Fig. 1c).

This confirms that the single positive peak occurs when the chromophores are closely packed allowing for a charge transfer process resulting in an oxidized and reduced species. The TA spectra were fitted with biexponentials, yielding time constants for the charge transfer processes occurring within the thin films, which can be found summarized in the ESI,† (Table S2). From there the corresponding spectra were extracted by a global fit (Fig. 4b–e). For more information on the global analysis and the global fitting procedure, the reader is directed to the ESI,† (S2) and the following literature.[32–34]

With increasing proportion of PMMA there is an increase in both of the time constants, and the rate constants for the different blends display a linear dependence with increasing PMMA ratio (Fig. 4f).

This helps us in confirming our hypothesis that the positive feature corresponds to photoinduced charge separation within the films, since the charge transfer kinetics are very sensitive to the intermolecular distance between the donor and the acceptor. Furthermore, Fig. 4b–e reveal that charge transfer occurs despite the fact that we radically change the degree of aggregation. Keeping the excitation wavelength at 580 nm, we change from exciting predominantly aggregates to monomers when the dye is diluted in PMMA.

These results allow us to propose two possible mechanisms for intrinsic charge generation in Cy5-P, both of which involve H-aggregates. The first reaction considers direct excitation of H-aggregates into higher energy exciton bands from where reductive quenching by the monomer species occurs (eqn (1)). On the other hand, charge transfer can proceed *via* electron transfer from the excited monomer species (eqn (2)). Both of these mechanisms generate the positive feature at 470 nm which is seen in the transient absorption spectrum.

$$\mathrm{Cy5} + \mathrm{(H)Cy5} + h\nu \rightarrow \mathrm{Cy5} + \mathrm{(H)Cy5^*} \rightarrow \mathrm{Cy5^+} + \mathrm{(H)Cy5^-} \quad (1)$$

$$\mathrm{Cy5} + \mathrm{(H)Cy5} + h\nu \rightarrow \mathrm{(H)Cy5} + \mathrm{Cy5^*} \rightarrow \mathrm{Cy5^+} + \mathrm{(H)Cy5^-} \quad (2)$$

The thermodynamic driving force has been proposed to arise from energetic disorder within the film.[35] Apart from energy level shifts arising from electronic coupling between dye molecules, local electric fields may also substantially shift the HOMO and LUMO energy levels of the cyanine chromophores. When the cyanine cations form H-aggregate stacks, the anions are situated on the outside of the positively charged stack, which could give rise to the aforementioned local electric field, and thus lowering the energy levels of the H-aggregates with respect to those of the monomeric species.

Once the charges have undergone separation onto well separated sites, the positively charged hole is subsequently shielded from recombination by the negatively charged anions which surround the aggregates, which should result in an increase in the charge carrier lifetime, as found previously but not seen in these measurements.[20] This difference can be explained by a much larger concentration of charge carriers produced at laser excitation intensity resulting in increased bimolecular charge carrier recombination and thus a much lower charge carrier lifetime than seen previously.

CC BY-NC

 This journal is © the Owner Societies 2021

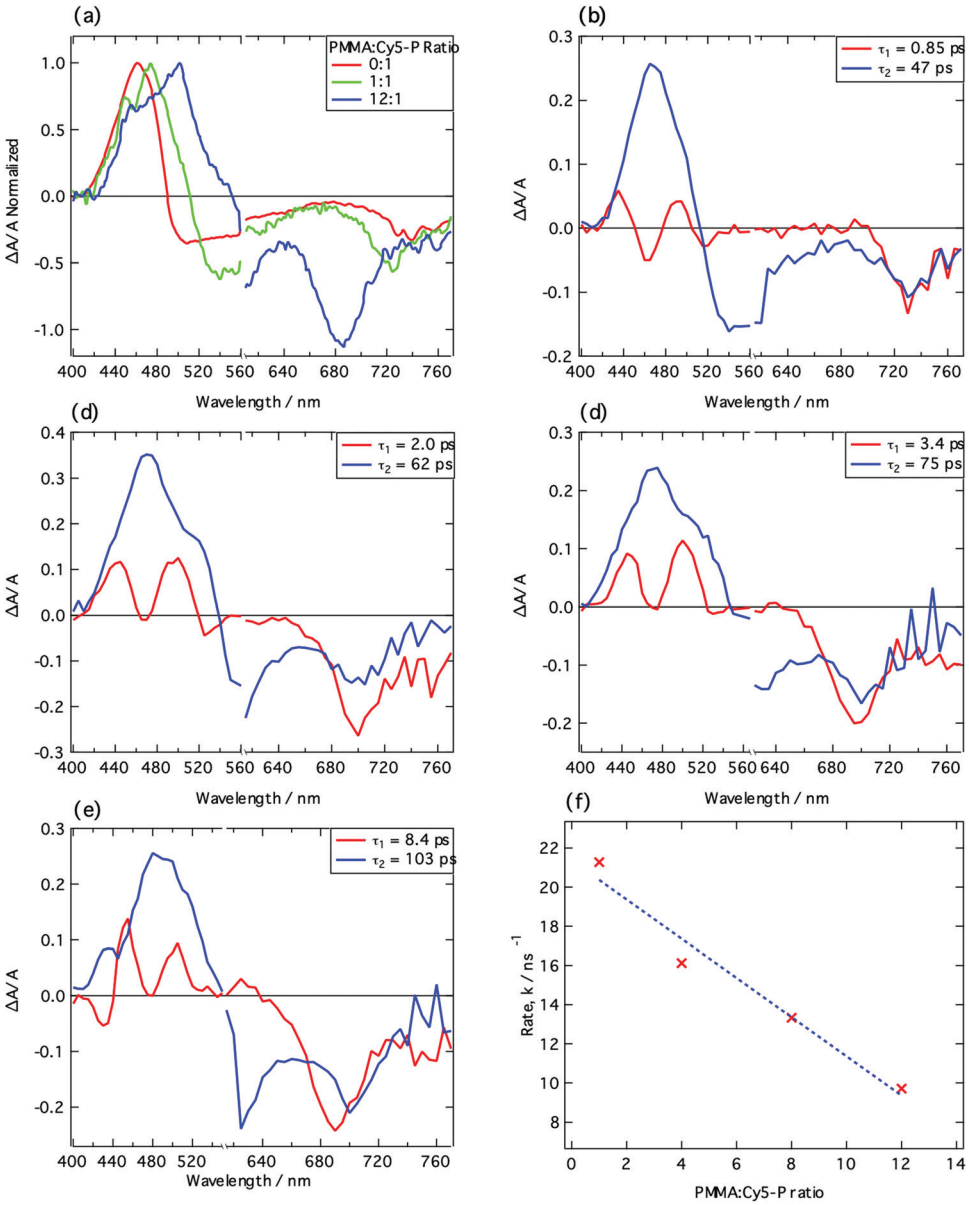

Fig. 4 (a) Normalized TA spectra for 0 : 1, 1 : 1 and 12 : 1 (mol : mol) blends of PMMA : Cy5-P at a time of 1 ps. Samples were excited at 580 nm with a fluence of 30 μJ cm^{-2}; (b)–(e) Global fits for different PMMA : Cy5-P blends (1 : 1, 4 : 1, 8 : 1 and 12 : 1); (f) Plot showing the rate of electron transfer as a function of PMMA : Cy5-P blend ratio.

CC BY-NC

Impact of the counterion

Having established the presence of aggregate oxidized species within the photoexcited film, the impact of the counterion on the charge generation process was investigated. Alongside the hexafluorophosphate anion (Volume of anion determined by X-ray diffraction, V^{-} = 0.093 nm^3), three other counterions were studied in combination with the same chromophore: chloride (Cy5-Cl; V^{-} = 0.029 nm^3), tetrakis(nonafluoro-*tert*-butoxy)aluminate (Cy5-[Al(pftb)$_4$]; V^{-} = 0.707 nm^3) and tetrakis(perfluoro-1-adamantoxy)aluminate (Cy5-[Al(pfad)$_4$]; V^{-} = 1.194 nm^3). Thus, V^{-} was changed by a factor of 41 if comparing Cy5-Cl with Cy5-[Al(pfad)$_4$].

The crystal structures of the PF_6^{-}, Al(pftb)$_4^{-}$ and Al(pfad)$_4^{-}$ salts were determined, and Hirshfeld analysis was conducted. An in-depth description of Hirshfeld surface analysis can be found here.[36] From the Hirshfeld surfaces, fingerprint plots were produced (Fig. S3.2, ESI†), which provide a visual summary of the intermolecular contacts within the crystal structures.[37] By examining the fingerprint plots of the H–H intermolecular contacts, it is evident that as the anion size increases the mean inter-chromophore distance increases. In addition, the dominating H–H intermolecular cation–cation contacts in Cy5-P (51.7% of the interactions) are replaced by others and the H–H cation–cation interactions only account for 13.6% of the contacts as a consequence of the now much larger counterion in Cy5-[Al(pfad)$_4$].

The increase in inter-chromophore distance results in a decrease in the degree of aggregation within the film, as shown

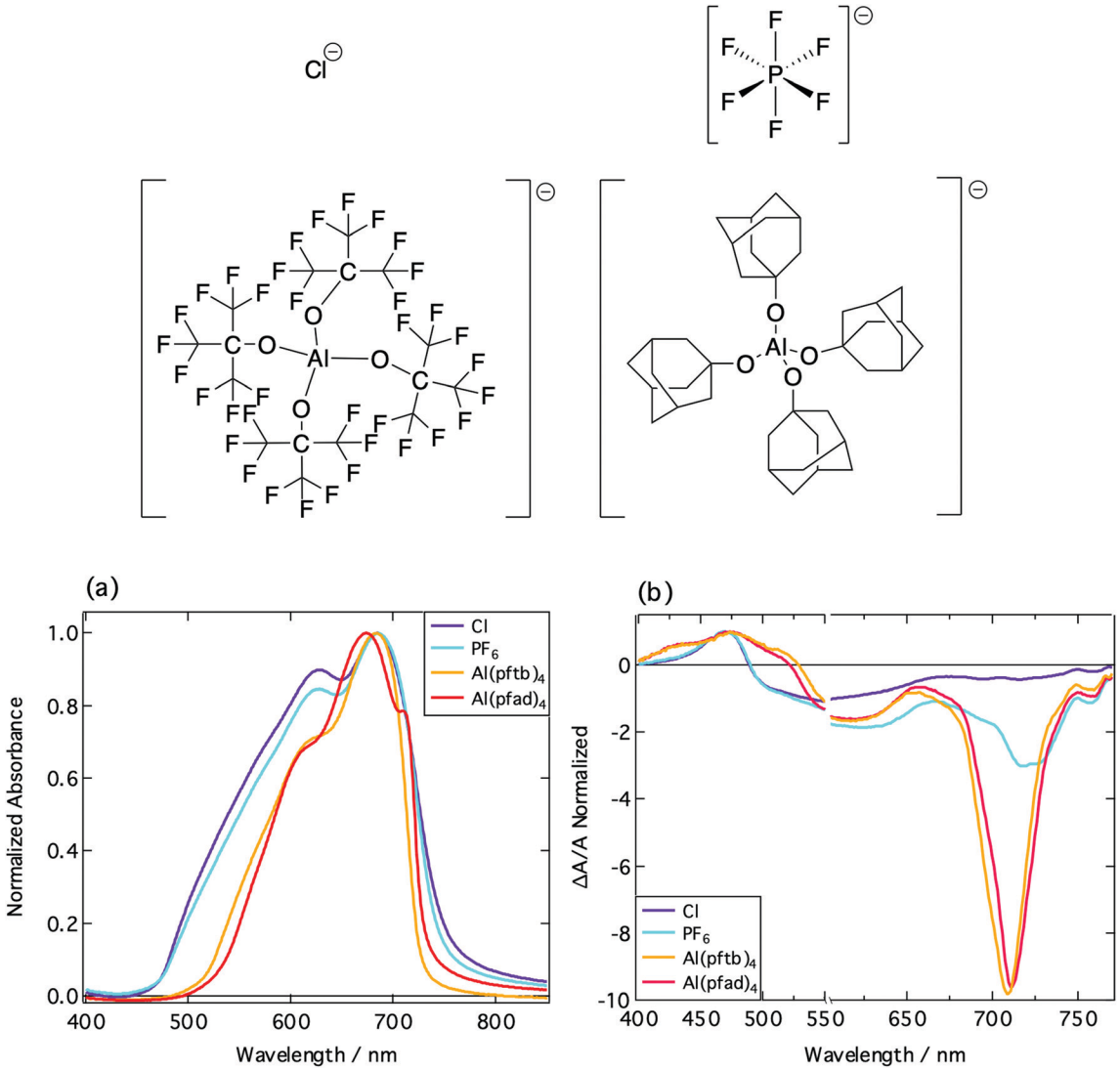

Fig. 5 Structures of the different anion counterions: Cl^-, PF_6^-, $Al(pftb)_4^-$ (left) and $Al(pfad)_4^-$ (right). Note that the fluorine atoms have been omitted from the $Al(pfad)_4^-$ structure for clarity. (a) Normalized absorption spectra of Cy5 thin films incorporating different counterions: Cl^- (purple), PF_6^- (cyano), $Al(pftb)_4^-$ (orange) and $Al(pfad)_4^-$ (red). (b) Normalized transient absorption spectra of different Cy5 thin films, taken at a time of 1 ps. Samples were excited at 580 nm.

by a decrease in the ratio of the H-dimer:monomer peak height, as well as the reduced FWHM (Fig. 5a). We note that the same features are observed for the absorption coefficient measured by ellipsometry (Fig. S4.2, ESI†). The anion size also impacts upon the transient absorption spectra of the thin films (Fig. 5b).

With increasing anion size, there is an increase in the relative intensity of the stimulated emission, arising due to a decrease in energetic disorder thus leading to a decrease in selfquenching.[38] Furthermore, as the anion size increases, there is a slight shift in the positive feature in the TA spectra at 470 nm, and a second feature begins to be resolved. This reflects a diminished bleaching contribution of the H-aggregates, in accordance with the results obtained for Cy5 dispersed in PMMA. The thin films fabricated were reproducible, and the absorption spectra identical between batches. This allows us to conclude that the differences in the photophysics between the dyes incorporating different counterions are due to the difference in aggregation, and not due to structural defects occurring during film formation.

Global fits of the transient spectra were obtained by fitting the spectra with three exponential functions, and these fits were then used to calculate the quantum yield for charge separation (S4 and S5, ESI†). The quantum yield of the charge separation process was found to be 83% and 86% for the Cy5-Cl and Cy5-P systems, respectively. This yield then decreased to 71% and 78% for the two aluminium-based analogues, Cy5-[$Al(pftb)_4$] and Cy5-[$Al(pfad)_4$].

The decrease in yield for the larger counterions further confirms that the interchromophore distance, and therefore the degree of aggregation, plays a key role in the charge transfer process. In the thin films of the cyanine dyes with the larger

BY-NC

 This journal is © the Owner Societies 2021

counterions ($Al(pftb)_4$ and $Al(pfad)_4$), the counterions are sufficiently large to ensure that higher order H-aggregates do not readily form, which minimises electron transfer from photoexcited monomer chromophores to the aggregates.

Charge transport

Having established a link between anion size and the mechanism of charge generation, the impact of the anion on charge transport was then investigated. For this, electroabsorption and time-resolved electroabsorption spectroscopy (TREAS) were used. These are spectroscopic techniques based upon the electric-field dependent optical response of a system (Stark effect).[18]

Experimentally, the difference between electroabsorption measurements and TREAS is the addition of a pump beam in the latter. This photoexcitation of the sample generates charge pairs, which undergo separation under the applied electric field causing changes in the electroabsorption response of the material. By monitoring the time evolution, the charge carrier mobility can be determined. For more details on these techniques, the reader is directed to the following literature.[18,39,40]

While the electroabsorption spectra of the Cy5 dyes have similar shapes (Fig. S6.1, ESI†), there is a clear red shift in the positive feature as the anions increase in size (from 475 nm in Cy5-Cl to 550 nm in Cy5-[$Al(pfad)_4$]). As the shape of the electroabsorption spectrum is related to the derivative of the absorption spectrum, this red shift arises from a decrease in higher order H-aggregates as the anion size increases. It is possible to determine the origin of certain features within the EA spectrum by comparing it to the derivatives of the steady state absorption spectrum. Furthermore, a linear combination of the zeroth, first and second derivatives can be fitted to the electroabsorption spectrum, with the accuracy of the fit determined by the number of transitions behind each absorption band.

The fits (Fig. S6.2, ESI†) for the Cy5-Cl and Cy5-P dyes are reasonably accurate; in contrast, however, the fits for the dyes with the two aluminium-based counterions are inaccurate. This implies that in these films there is inhomogeneity in the polarizability and the permanent dipole on a short length scale (tens of nm) and that the film is locally disordered. Furthermore, any aggregates that are present in these films do not exhibit uniform properties.[41]

The results from the TREAS experiments proved inconclusive. This was caused by the poor carrier mobility resulting in there being little time evolution in the electroabsorption spectra over the time-window of the experiment (approximately 1.6 ns). As the films of the cyanine dyes were already very thin (20–50 nm), decreasing the film thickness or increasing the applied voltage were not feasible solutions. As a result, time-of-flight (TOF) was instead used to estimate the impact of anion size on charge carrier mobility.

TOF is a technique whereby electron–hole pairs are generated in an electric field upon photoexcitation of the sample in the immediate vicinity of one electrode. The electric field then splits the electron–hole pair, where one charge is immediately collected by the nearby electrode, while the other traverses the sample to be collected at the counter electrode. The time taken for these charges to traverse the sample is called the transit time, and it can be used to calculate the charge mobility in the sample using the following equation:

$$\mu = \frac{d^2}{E \cdot t_{tr}} \tag{3}$$

where d is the sample thickness, E the voltage applied across the sample and t_{tr} the transit time obtained from the TOF measurements.

As well as giving the charge mobility in the sample, TOF can also give insight into the transport regime (dispersive *vs.* non-dispersive), by means of the appearance of the photocurrent curve. The mobility of the Cy5 dyes with the two smaller counterions (Cl^- and PF_6^-) were investigated alongside [$Al(pftb)_4$].

Samples were excited at 630 nm with an applied voltage of 8 V. An example of the resulting photocurrent curve is shown in the ESI† (Fig. S6.3). The transit time was estimated from the curve by constructing asymptotes with the intersection corresponding to the transit time.[42] The thickness of the samples was determined by using cross-sectional scanning electron microscopy (Fig. 6 and Fig. S7, ESI†).

As evident from Table 1, the mobility values are similar irrespective of the counterion size, and are comparable to those found in organic salt photovoltaics.[43,44] This is an interesting result, as one would expect there to be a decrease in mobility as the anion size increases as a result of the chromophores being further apart, reducing the rate of charge hopping.

However, while the average separation of the Cy5 chromophores increases with increasing anion size and the percentage of interacting cation–cation surfaces is reduced by a factor of 4 (from 51.7 to 13.6%), the sections of the cations that mitigate

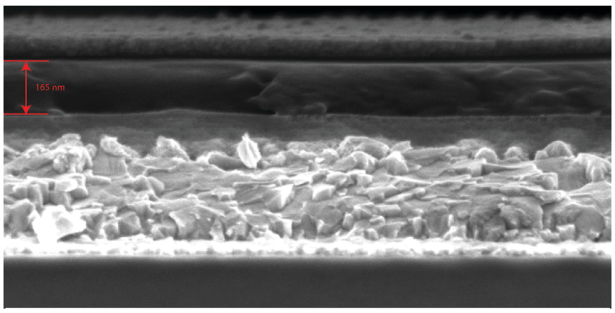

Fig. 6 Cross-sectional scanning electron microscopy (SEM) image of Cy5-[$Al(pftb)_4$] time of flight sample. Sample comprises of glass/FTO/Al_2O_3/Cy5-[$Al(pftb)_4$]/Al.

Table 1 Transit times and mobility values for different Cy5 salts

Anion	Transit time/μs	Mobility/10^{-6} cm^2 V^{-1} s^{-1}	Thickness/nm
Cl^-	2.47 ± 0.04	6.12 ± 0.09	110
PF_6^-	2.75 ± 0.13	3.69 ± 0.18	90
$Al(pftb)_4^-$	5.92 ± 0.30	5.75 ± 0.29	165

This journal is © the Owner Societies 2021

charge transfer remain in contact. Therefore, even with the largest anions, it is not possible to break the interaction paths through the entire film.

Overall, the result is that the carrier mobility of the dyes with larger anions is similar to that of the dyes with smaller counterions, as the larger inter-chromophore distance is countered by the decreased degree of aggregation, and subsequent minimization of charge trapping by H-aggregates. Due to limitations with the sample preparation, it was difficult to get sufficiently thick samples to be able to conclusively determine the transport regime (dispersive *vs.* non-dispersive); furthermore, these limitations lead to a certain degree of uncertainty in regard to the mobility values found. However, while the absolute values may not be correct, we believe that the mobility values of the three dye materials tested are similar, and so the conclusions we have drawn are still valid.

Conclusions

In summary, we have shown using transient absorption spectroscopy that oxidized monomer species are photogenerated in pentamethine cyanine dye films incorporating small counterions, such as chloride or hexafluorophosphate. This has allowed us to confirm the charge generation mechanism in these materials, providing the first direct proof of high efficiency intrinsic charge generation in organic salt semiconductors. Upon photoexcitation, charge pairs are generated with the electron undergoing transfer from singlet excited states of monomeric species in the film to ground state aggregated chromophores. Alternatively, direct excitation of H-aggregates can occur, followed by reductive quenching by the monomer species. These charge transfer processes occur with a yield of up to 86%. The involvement of H-aggregates in the photoinduced charge separation process is essential as it ensures the necessary symmetry-breaking[45,46] and the thermodynamic driving force to yield the charge separated pair.

The impact of counterion size was then examined, with dyes containing two very large aluminium based counterions, Cy5-[Al(pftb)$_4$] and Cy5-[Al(pfad)$_4$], being studied alongside Cy5-Cl and Cy5-P. Transient absorption measurements demonstrated that monomer oxidized species were less present in the samples containing the two larger anions or samples where the cyanine dye was diluted in a polymer matrix. These results led us to conclude that in pentamethine cyanine dyes, where the anion is sufficiently large, higher order H-aggregates are not present in high concentration due to the chromophores being too spatially separated, thus diminishing the process of charge generation. However, despite an increase in spatial separation, time of flight measurements showed that the carrier mobility in Cy5-Al(pftb)$_4$ was similar to that of the Cy5 dyes with the smaller counterions. This is interpreted as a counterbalancing effect for the charge carrier mobility, where the increased interchromophore distance in Cy5-[Al(pftb)$_4$] films is compensated by the decrease in energetic disorder due to the suppression of H-aggregates.

Author contributions

All authors have given approval to the final version of the manuscript.

Conflicts of interest

The authors declare no conflict of interest.

Acknowledgements

Financial support by the Swiss National Science Foundation (SNF, Grant no. 200021_175729) and the National Center of Competence in Research ''Molecular Ultrafast Science and Technology'' (NCCR-MUST), a research instrument of the SNF, is gratefully acknowledged. The authors thank Linfeng Pan for cross-sectional SEM images, as well as Karen Strassel and Matthias Diethelm for their help in thin film preparation. Roland Hany is acknowledged for helpful discussions.

References

1 M. Bates and R. R. Lunt, *Sustainable Energy Fuels*, 2017, **1**, 955–968.
2 R. Hany, B. Fan, F. Araujo De Castro, J. Heier, W. Kylberg and F. Nüesch, *Prog. Photovoltaics*, 2011, **19**, 851–857.
3 E. Berner, T. Jäger, T. Lanz, F. Nüesch, J. N. Tisserant, G. Wicht, H. Zhang and R. Hany, *Appl. Phys. Lett.*, 2013, **102**, 98–102.
4 B. Siegmund, M. T. Sajjad, J. Widmer, D. Ray, C. Koerner, M. Riede, K. Leo, I. D. W. Samuel and K. Vandewal, *Adv. Mater.*, 2017, **29**, 3–7.
5 J. J. M. Halls, C. A. Walsh, N. C. Greenham, E. A. Marseglia, R. H. Friend, S. C. Moratti and A. B. Holmes, *Nature*, 1995, **376**, 498–500.
6 A. C. Véron, H. Zhang, A. Linden, F. Nüesch, J. Heier, R. Hany and T. Geiger, *Org. Lett.*, 2014, **16**, 1044–1047.
7 H. Zhang, G. Wicht, C. Gretener, M. Nagel, F. Nüesch, Y. Romanyuk, J. N. Tisserant and R. Hany, *Sol. Energy Mater. Sol. Cells*, 2013, **118**, 157–164.
8 D. Gesevičius, A. Neels, S. Jenatsch, E. Hack, L. Viani, S. Athanasopoulos, F. Nüesch and J. Heier, *Adv. Sci.*, 2018, **5**, 1700496.
9 D. Gesevičius, A. Neels, S. Yakunin, E. Hack, M. V. Kovalenko, F. Nüesch and J. Heier, *ChemPhysChem*, 2018, **19**, 3356–3363.
10 I. Krossing and I. Raabe, *Angew. Chem., Int. Ed.*, 2004, **43**, 2066–2090.
11 I. M. Riddlestone, A. Kraft, J. Schaefer and I. Krossing, *Angew. Chem., Int. Ed.*, 2018, **57**, 13982–14024.
12 A. Rupp, N. Roznyatovskaya, H. Scherer, W. Beichel, P. Klose, C. Sturm, A. Hoffmann, J. Tübke, T. Koslowski and I. Krossing, *Chem. – Eur. J.*, 2014, **20**, 9794–9804.
13 A. B. A. Rupp and I. Krossing, *Acc. Chem. Res.*, 2015, **48**, 2537–2546.

BY-NC

 This journal is © the Owner Societies 2021

14 F. Nüesch, A. Faes, L. Zuppiroli, F. Meng, K. Chen and H. Tian, *J. Mater. Sci.*, 2005, **40**, 1353–1357.
15 O. Malinkiewicz, T. Grancha, A. Molina-Ontoria, A. Soriano, H. Brine and H. J. Bolink, *Adv. Energy Mater.*, 2013, **3**, 472–477.
16 Z. Huang, D. Ji, S. Wang, A. Xia, F. Koberling, M. Patting and R. Erdmann, *J. Phys. Chem. A*, 2006, **110**, 45–50.
17 C. A. Guarin, J. P. Villabona-Monsalve, R. López-Arteaga and J. Peon, *J. Phys. Chem. B*, 2013, **117**, 7352–7362.
18 A. Devižis, A. Gelzinis, J. Chmeliov, M. Diethelm, L. Endriukaitis, D. Padula and R. Hany, *Adv. Funct. Mater.*, 2021, **2102000**, 1–8.
19 J. De Jonghe-Risse, J. Heier, F. Nüesch and J.-E. Moser, *J. Mater. Chem. A*, 2015, **3**, 10935–10941.
20 L. Wang, S. Jenatsch, B. Ruhstaller, C. Hinderling, D. Gesevičius, R. Hany and F. Nüesch, *Adv. Funct. Mater.*, 2018, **28**, 1–8.
21 M. Young, J. Suddard-Bangsund, T. J. Patrick, N. Pajares, C. J. Traverse, M. C. Barr, S. Y. Lunt and R. R. Lunt, *Adv. Opt. Mater.*, 2016, **4**, 1028–1033.
22 Y. Yang, S. Omi, R. Goto, M. Yahiro, M. Era, H. Watanabe and Y. Oki, *Org. Electron.*, 2011, **12**, 405–410.
23 T. P. Osedach, A. Iacchetti, R. R. Lunt, T. L. Andrew, P. R. Brown, G. M. Akselrod and V. Bulović, *Appl. Phys. Lett.*, 2012, **101**, 113303.
24 Y. Yang, T. Nakamichi, H. Yoshioka, M. Yahiro, M. Era, H. Watanabe, Y. Cui, Y. Oki and G. Qian, *J. Mater. Chem. C*, 2013, **1**, 1739–1744.
25 S. B. Anantharaman, K. Strassel, M. Diethelm, A. Gubicza, E. Hack, R. Hany, F. A. Nüesch and J. Heier, *J. Mater. Chem. C*, 2019, **7**, 14639–14650.
26 A. L. Mannanov, P. S. Savchenko, Y. N. Luponosov, A. N. Solodukhin, S. A. Ponomarenko and D. Y. Paraschuk, *Org. Electron.*, 2020, **78**, 105588.
27 H. T. Chandran, T. W. Ng, Y. Foo, H. W. Li, J. Qing, X. K. Liu, C. Y. Chan, F. L. Wong, J. A. Zapien, S. W. Tsang, M. F. Lo and C. S. Lee, *Adv. Mater.*, 2017, **29**, 1606909.
28 W. Li, D. Li, G. Dong, L. Duan, J. Sun, D. Zhang and L. Wang, *Laser Photonics Rev.*, 2016, **10**, 473–480.
29 E. N. Kaliteevskaya, V. P. Krutyakova, T. K. Razumova and A. A. Starovoitov, *Opt. Spectrosc.*, 2016, **120**, 482–491.
30 S. Chatterjee, B. Sauerwein, X. Yang, G. B. Schuster, P. D. Davis, P. Gottschalk and M. E. Kurz, *J. Am. Chem. Soc.*, 1990, **112**, 6329–6338.
31 J. R. Lenhard and A. D. Cameron, *J. Phys. Chem.*, 1993, **97**, 4916–4925.
32 I. H. M. Van Stokkum, D. S. Larsen and R. Van Grondelle, *Biochim. Biophys. Acta, Bioenerg.*, 2004, **1657**, 82–104.
33 R. Berera, R. van Grondelle and J. T. M. Kennis, *Photosynth. Res.*, 2009, **101**, 105–118.
34 M. E. F. Bouduban, A. Burgos-Caminal, R. Ossola, J. Teuscher and J.-E. Moser, *Chem. Sci.*, 2017, **8**, 4371–4380.
35 U. B. Cappel, D. Moia, A. Bruno, V. Vaissier, S. A. Haque and P. R. F. Barnes, *Sci. Rep.*, 2016, **6**, 1–9.
36 M. A. Spackman and D. Jayatilaka, *CrystEngComm*, 2009, **11**, 19–32.
37 M. A. Spackman and J. J. McKinnon, *CrystEngComm*, 2002, **4**, 378–392.
38 D. Oelkrug, H. J. Egelhaaf, J. Gierschner and A. Tompert, *Synth. Met.*, 1996, **76**, 249–253.
39 A. A. Paraecattil, J. De Jonghe-Risse, V. Pranculis, J. Teuscher and J.-E. Moser, *J. Phys. Chem. C*, 2016, **120**, 19595–19602.
40 M. F. Bouduban, A. Burgos-Caminal, J. Teuscher and J.-E. Moser, *Chimia*, 2017, **71**, 231–235.
41 A. Chowdhury, S. Wachsmann-Hogiu, P. R. Bangal, I. Raheem and L. A. Peteanu, *J. Phys. Chem. B*, 2001, **105**, 12196–12201.
42 N. A. Mica, S. A. J. Thomson and I. D. W. Samuel, *Org. Electron.*, 2018, **63**, 415–420.
43 S. Jenatsch, R. Hany, A. Véron, M. Neukom, S. Zufle, A. Borgschulte, B. Ruhstaller and F. Nüesch, *J. Phys. Chem. C*, 2014, **118**, 17036.
44 M. Bates and R. R. Lunt, *Sustainable Energy Fuels*, 2017, **1**, 195.
45 E. Vauthey, *Chem. Phys. Chem.*, 2012, **13**, 2001–2011.
46 C. E. Ramirez, S. Chen, N. E. Powers-Riggs, I. Schlesinger, R. M. Young and M. R. Wasielewski, *J. Am. Chem. Soc.*, 2020, **142**, 18243–18250.

BY-NC

Electronic Supplementary Material (ESI) for Physical Chemistry Chemical Physics.
This journal is © the Owner Societies 2021

Supplementary Information

Critical Role of H-Aggregation for High-Efficiency Photoinduced Charge Generation in Pristine Pentamethine Cyanine Salts

George C. Fish,[a] Juan Manuel Moreno-Naranjo,[a†] Andreas Billion,[b] Daniel Kratzert,[b] Erwin Hack,[c] Ingo Krossing,[b] Frank Nüesch[d,e] and Jacques-E. Moser*[a]

a) *Photochemical Dynamics Group, Institute of Chemical Sciences and Engineering, École polytechnique fédérale de Lausanne, Station 6, 1015 Lausanne, Switzerland.*

b) *Institut für Anorganische und Analytische Chemie, and Freiburger Materialforschungszentrum, Universität Freiburg, Albertstrasse 21, 79104 Freiburg, Germany.*

c) *Laboratory for Transport at Nanoscale Interfaces, Swiss Federal Laboratories for Materials Science and Technology, Empa, Überlandstrasse 129, 8600 Dübendorf, Switzerland.*

d) *Laboratory for Functional Polymers, Swiss Federal Laboratories for Materials Science and Technology, Empa, Überlandstrasse 129, 8600 Dübendorf, Switzerland.*

e) *Institute of Materials, School of Engineering, École polytechnique fédérale de Lausanne, Station 12, 1015 Lausanne, Switzerland.*

† Current address: Department of Chemistry, Molecular Sciences Research Hub, Imperial College London, White City Campus, London, W12 OBZ, United Kingdom

* *Corresponding author. Email: je.moser@epfl.ch*

S1. Synthetic Procedure for the preparation of Cy5-[Al(pftb)$_4$] and Cy5-[Al(pfad)$_4$]

General Working Technique

All manipulations were carried out under an inert argon atmosphere, using standard vacuum and Schlenk techniques with a pressure of 10^{-3} mbar or a glove box (MBraun Lab Master) with argon atmosphere and H_2O and O_2 contents <1 ppm to exclude air and moisture. All solvents and reagents were dried using conventional drying agents, distilled afterwards and stored under argon atmosphere over activated 3 Å molecular sieves.

NMR Spectroscopic Investigations

NMR samples were prepared in an inert atmosphere glove box in NMR tubes equipped with a gas-tight J. Young valve. NMR spectra were recorded on a Bruker Avance II$^+$ 400 MHz WB and a Bruker Avance III HD 300 MHz NMR spectrometer at room temperature (unless described otherwise) using the software package Bruker TopSpin 4.0.7 for analysis. The spectra were calibrated based on the chemical shift of the deuterated solvents used.

Single Crystal X-ray Diffraction

The data was collected from shock-cooled single crystals at 100(2) K on a Bruker D8 VENTURE dual wavelength Mo/Cu three-circle diffractometer with a microfocus sealed X-ray tube using mirror optics as monochromator and a Bruker PHOTON III detector. The diffractometer was equipped with an Oxford Cryostream 800 low temperature device and used MoK_α radiation (λ = 0.71073 Å). All data were integrated with SAINT and a multi-scan absorption correction using SADABS was applied.[1,2] The structure were solved by direct methods using SHELXT and refined by full-matrix least-squares methods against F^2 by SHELXL-2018/3.[3,4] All non-hydrogen atoms were refined with anisotropic displacement parameters. The hydrogen atoms were refined isotropically on calculated positions using a riding model with their U_{iso} values constrained to 1.5 times the U_{eq} of their pivot atoms for terminal sp^3 carbon atoms and 1.2 times for all other carbon atoms. Crystallographic data for the structures reported in this paper have been deposited with the Cambridge Crystallographic Data Centre.[5] CCDC 2044614 and 2056417 contain the supplementary crystallographic data for this paper. These data can be obtained free of charge from The Cambridge Crystallographic Data Centre via www.ccdc.cam.ac.uk/structures. This report and the CIF file were generated using FinalCif.[6]

S1.1 Synthesis and Characterization of the [Cy5][Al(pftb)$_4$] (pftb = OC(CF$_3$)$_3$)

Li[Al(OC(CF$_3$)$_3$)$_4$] (1.092 g, 1.121 mmol) and [Cy5][BF$_4$] (0.521 g, 1.108 mmol, 1.00 eq) were submitted into a H-cell equipped with a G4 frit and dissolved in CH_2Cl_2 (10 mL) and stirred at r.t. for 3 days. The reaction mixture was sonicated for 1 h and filtered after the precipitation of solid could be observed. The solvent was removed under reduced pressure und the title compound was isolated as blue powder (1.23 g, 0.911 mmol, 82 %) and characterized by NMR spectroscopy.

Recorded NMR spectra of [Cy5][Al(OC(CF$_3$)$_3$)$_4$] in CD_2Cl_2, $CDCl_3$ and *o*-DFB always showed heavily broadened resonances in the ^{1}H-NMR spectra in contrast to the reference spectrum of [Cy5][BF$_4$] (Figure S1.1). These broadened resonances in the regions of 2.37 to 4.80 and 5.80 to 8.50 ppm show no clear splitting pattern but are the main resonances and caused by [Cy5][Al(OC(CF$_3$)$_3$)$_4$]. A precise assignment of the resonances of the title compound is not possible due to the enlargement with exception of the intensive singlet at 1.71 ppm caused by the CH_3 groups (H8)) of [Cy5][Al(OC(CF$_3$)$_3$)$_4$]. The ^{1}H-NMR spectrum further shows

resonances, which can be assigned to indoline moieties (Ind1, In2, **Erreur ! Source du renvoi introuvable.**S1.2) which indicate a partial decomposition of the cation [Cy5] but only represent 1 % of the intensity in the NMR sample. The assignment of the resonances of the decomposition products were completed, considering the ^{1}H,^{13}C-HSQC and ^{1}H,^{13}HMBC NMR spectra in Figures S1.3 and S1.4. The complete assignment is summarized in Table S1.1 and visualized in Figure S1.2.

Starting material [Cy5][BF$_4$] – reference NMR spectrum

^{1}H-NMR (400.17 MHz, 298 K, CDCl$_3$): δ = 1.68 (s, 12H, H(8)), 3.59 (s, 6H, H(13)), 6.15 (d, $^{3}J_{H,H}$ = 13.5 Hz, 2H, H(10)), 6.61 (t, $^{3}J_{H,H}$ = 12.5 Hz, 1H, H(12), 7.11 (d, $^{3}J_{H,H}$ = 8.1 Hz, 2H, H(2)), 7.18 (t, $^{3}J_{H,H}$ = 7.5 Hz, 2H, H(4)), 7.33 (m, 4H, H(5), H(3)), 8.02 (dd, $^{3}J_{H,H}$ = 13.3 Hz, 2H, H(11)) ppm.

^{11}B-NMR (128.39 MHz, 298 K, CDCl$_3$): δ = −0.7 (br. s, 1B, **B**F$_4$) ppm.

^{13}C-NMR (100.62 MHz, 298 K, CDCl$_3$): δ = 27.8 (C8), 31.4 (C13), 49.6 (C7), 103.6 (C10), 110.5 (C2), 122.2 (C5), 125.1 (C12), 126.0 (C4), 128.7 (C3), 141.3 (C6), 142.8 (C1), 154.1 (C11), 173.7 (C9) ppm.

^{19}F-NMR (376.54 MHz, 298 K, CDCl$_3$): δ = −152.0 (q, $^{2}J_{F,B}$ = 0.9 Hz, B^{11}**F**, 4F, [BF$_4$]$^-$), −151.9 (m, B^{10}**F**, 4F, [BF$_4$]$^-$) ppm.

[Cy5][Al(OC(CF$_3$)$_3$)$_4$]

^{1}H-NMR (400.17 MHz, 298 K, CDCl$_3$): δ = 1.68 (s, 6H, H(8)-Ind1), 1.71 (s, 12H, H(8)), 1,72(s, 6H, H(8)-Ind2), 2.37-4.80 (very broadened resonance, 6H, H(13)), 4.01 (br. s, 3H, H(10)-Ind2), 4.07 (br. s, 3H, H(10)-Ind1), 5.80-8.50 (very broadened resonance, 13H, H(10), H(12), H(2), H(4), H(5), H(3), H(11) ppm.

^{13}C-NMR (100.62 MHz, 298 K, CDCl$_3$): δ = 21.9 (C8-Ind1), 25.6 (C8-Ind2), 34.3 (C10-Ind2), 35.2 (C10-Ind1), 53.4 (C7-Ind1), 53.6 (C7-Ind2), 140.6 (C1-Ind2), 140.9 (C1-Ind1), 141.0 (C6-Ind1), 143.0 (C6-Ind2), 181.9 (C9-Ind2), 192.4 (C9-Ind1) ppm.

^{19}F-NMR (376.54 MHz, 298 K, CDCl$_3$): δ = −75.7 (s, 36F, [Al(OC(C**F$_3$**)$_3$)$_4$]$^-$) ppm.

^{27}Al-NMR (104.27 MHz, 298 K, CDCl$_3$): δ = 34.6 (s, 1Al, [**Al**(OC(CF$_3$)$_3$)$_4$]$^-$) ppm.

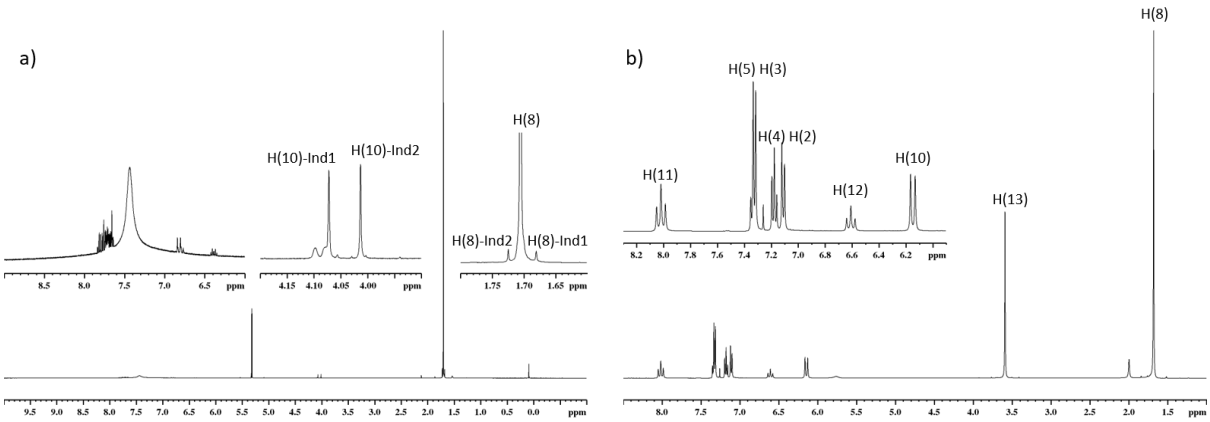

Figure S1.1. a) ^{1}H-NMR spectrum (400.17 MHz, 298 K, $CDCl_3$) Synthesis of [Cy5][Al(OC(CF_3)$_3$)$_4$] showing very small impurities by indoline species. b) ^{1}H-NMR spectrum (400.17 MHz, 298 K, $CDCl_3$) Reference spectrum of [Cy5][BF_4].

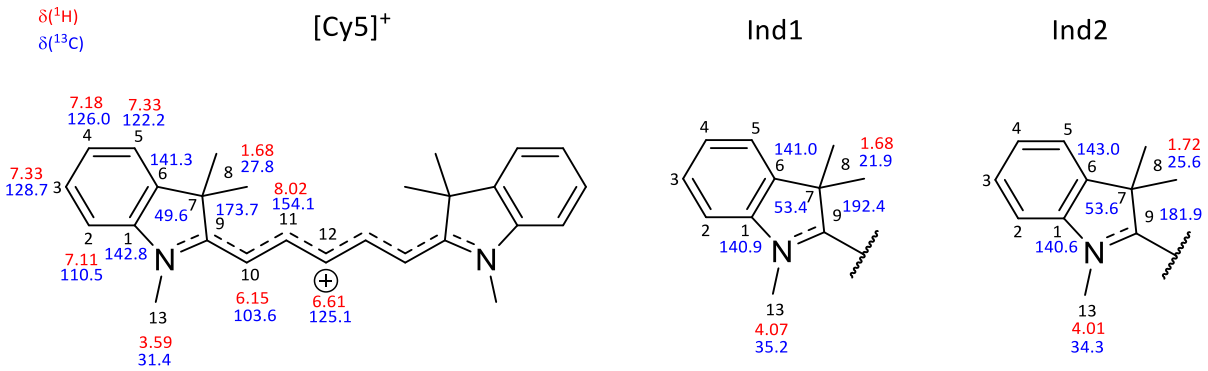

Figure S1.2. Assignment of the ^{1}H and ^{13}C chemical shifts of [Cy5][BF_4], Ind1 and In2.

Table S1.1. Overview of the ^{1}H and ^{13}C chemical shifts of [Cy5][BF_4], Ind1 and Ind2.

	[Cy5][BF_4]		Ind1		Ind2	
Position	δ(^{1}H)	δ(^{13}C)	δ(^{1}H)	δ(^{13}C)	δ(^{1}H)	δ(^{13}C)
1		142.8		140.9		140.6
2	7.11	110.5				
3	7.33	128.7				
4	7.18	126.0				
5	7.33	122.2				
6		141.3		141.0		143.0
7		49.6		53.4		53.6
8	1.68	27.8	1.68	21.9	1.72	25.6
9		173.7		192.4		181.9
10	6.15	103.6				
11	8.02	154.1				
12	6.61	125.1				
13	3.59	31.4	4.07	35.2	4.01	34.3

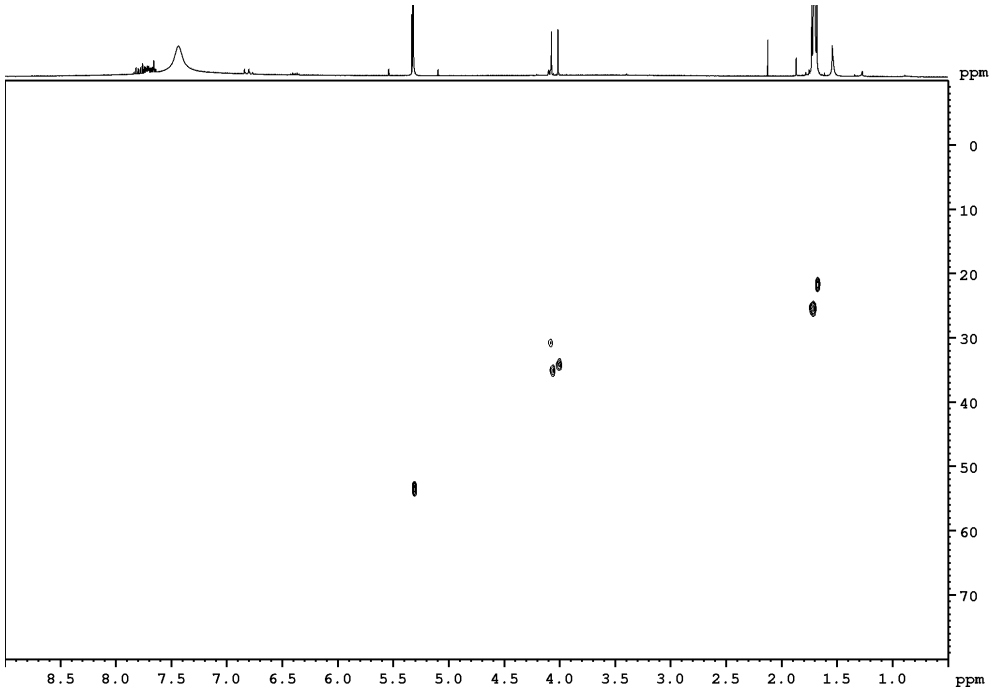

Figure S1.3. $^{1}H,^{13}C$-HSQC NMR spectrum (400.17 MHz, optimized on 1 Hz, 298 K, CD_2Cl_2) of the synthesis of $[Cy5][Al(OC(CF_3)_3)_4]$.

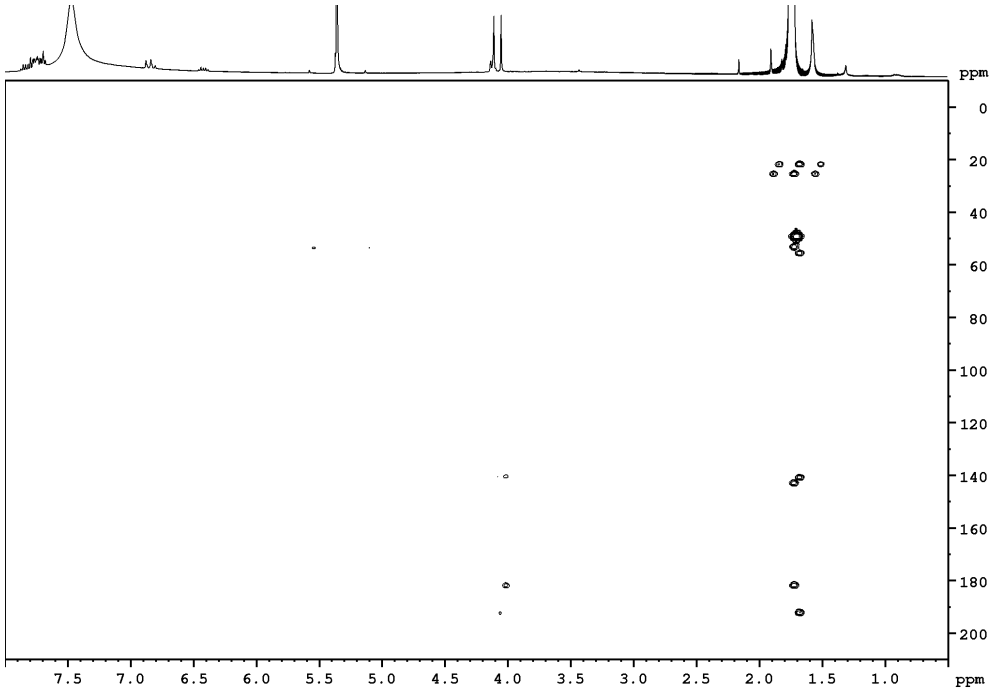

Figure S1.4. $^{1}H,^{13}C$-HMBC NMR spectrum (400.17 MHz, optimized on 8 Hz, 298 K, CD_2Cl_2) of the synthesis of $[Cy5][Al(OC(CF_3)_3)_4]$.

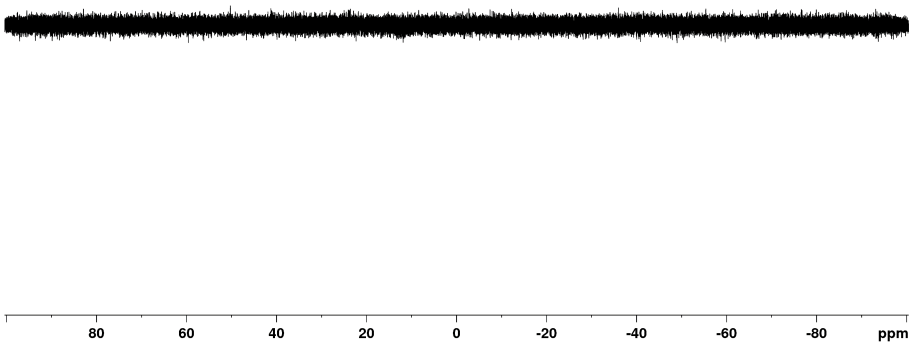

Figure S1.5. ^{7}Li-NMR spectrum (155.52 MHz, 298 K, $CDCl_3$) of the synthesis of [Cy5][Al(OC(CF_3)$_3$)$_4$]. Li^+ is absent.

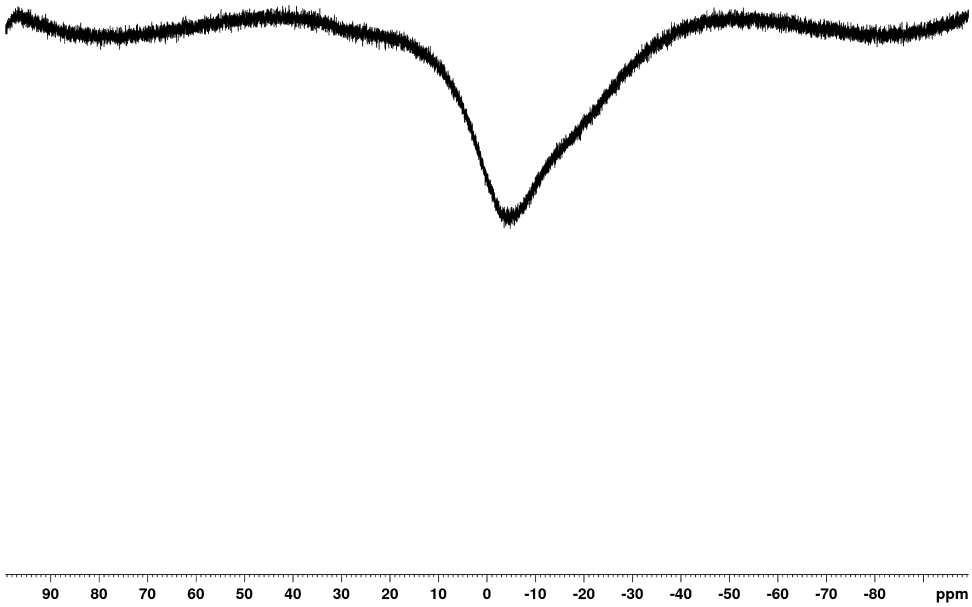

Figure S1.6. ^{11}B-NMR spectrum (128.39 MHz, 298 K, $CDCl_3$) of the synthesis of [Cy5][Al(OC(CF_3)$_3$)$_4$]. BF_4^- is absent.

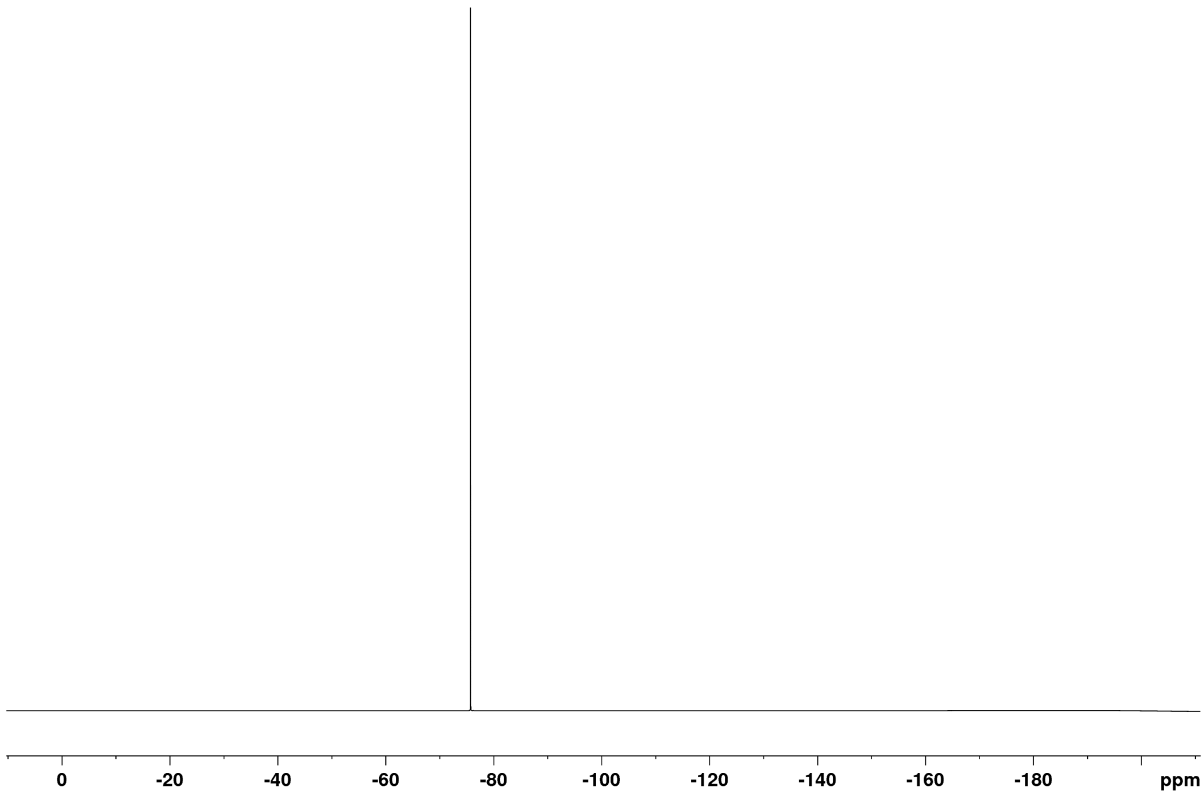

Figure S1.7. ^{19}F-NMR spectrum (376.54 MHz, 298 K, $CDCl_3$) of the synthesis of [Cy5][Al(OC(CF_3)$_3$)$_4$].

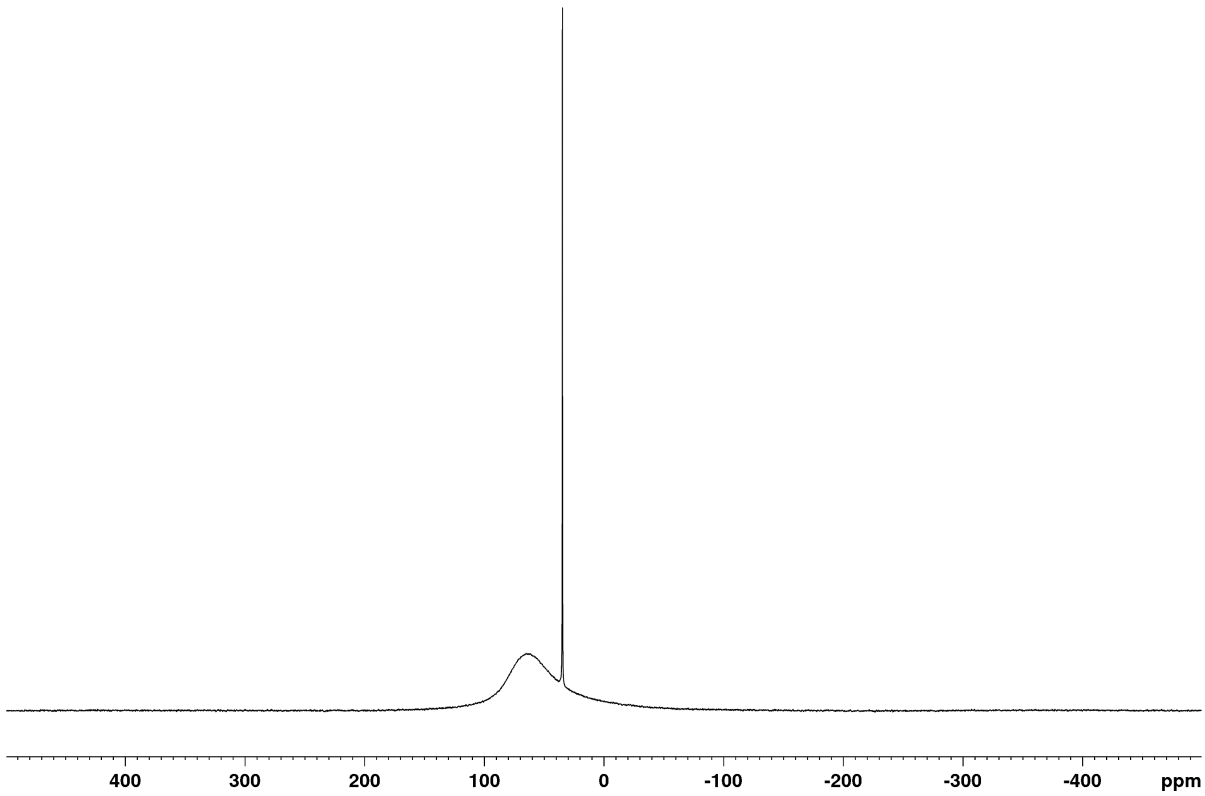

Figure S1.8. ^{27}Al-NMR spectrum (104.27 MHz, 298 K, $CDCl_3$) of the synthesis of [Cy5][Al(OC(CF_3)$_3$)$_4$].

S1.2. Synthesis and Characterization of the [Cy5][Al(pfad)$_4$] (pfad = perfluoroadamantoxy = $OC_{10}F_{15}$)

Li[Al($OC_{10}F_{15}$)$_4$] (0.650 g, 0.378 mmol) and [Cy5][BF_4] (0.181 g, 0.385 mmol, 1.02 eq) were submitted into a H-cell equipped with a G4 frit und dissolved in CH_2Cl_2 (10 mL) and stirred for 2 days at r.t. The reaction mixture was sonicated for 20 h and filtered after the precipitation of solid could be observed. The solvent was removed under reduced pressure und the title compound was isolated as green powder. NMR investigations showed impurities by $C_{10}F_{15}OH/C_{10}F_{15}O^-$. The obtained solid was dissolved in CH_2Cl_2 (10 mL) and suitable crystals for single crystal XRD experiments were obtained by slow vapor diffusion with *n*-pentane. After single crystal XRD experiments were done, the reaction solution was filtered, the crystalline residue washed with *n*-pentane (2x 4.0 mL) and dried in *vacuo*. The pure target compound was isolated as a yellow gleaming solid (0.20 g, 0.095 mmol, 25.0 %) and characterized by NMR spectroscopy.

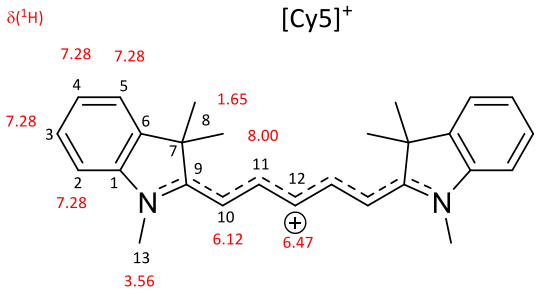

^{1}H-NMR (300.18 MHz, 298 K, THF/$CDCl_3$): δ = 1.65 (s, 12H, H(8)), 3.56 (s, 6H, H(13)), 6.12 (d, $^3J_{H,H}$ = 13.8 Hz, 2H, H(10)), 6.47 (t, $^3J_{H,H}$ = 12.5 Hz, 1H, H(12), 7.28 (m, 8H, H(2), H(4) H(5), H(3)), 8.00 (dd, $^3J_{H,H}$ = 13.0 Hz, 2H, H(11)) ppm.

^{19}F-NMR (282.45 MHz, 298 K, THF/$CDCl_3$): δ = −223.7 (s, C**F**, 12F, [Al($OC_{10}F_{15}$)$_4$]$^-$), −122.0 (m, C**F$_2$**, [Al($OC_{10}F_{15}$)$_4$]$^-$), −121.7 (m, C**F$_2$**, [Al($OC_{10}F_{15}$)$_4$]$^-$) ppm.

^{27}Al-NMR (78.22 MHz, 298 K, THF/$CDCl_3$): δ = 34.2 (s, 1Al, [**Al**($OC_{10}F_{15}$)$_4$]$^-$) ppm.

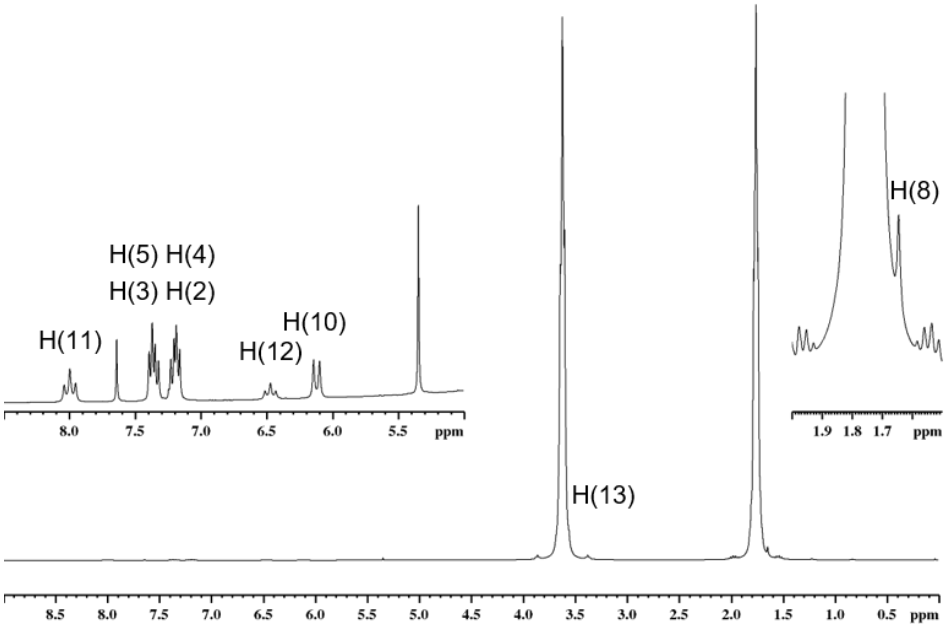

Figure S1.9. ^{1}H-NMR spectrum (300.18 MHz, 298 K, THF/$CDCl_3$) Synthesis of [Cy5][Al(pfad)$_4$] by reaction of Li[Al(pfad)$_4$] with [Cy5][BF_4] in CH_2Cl_2 after crystallization with n-pentane, calibrated on THF.

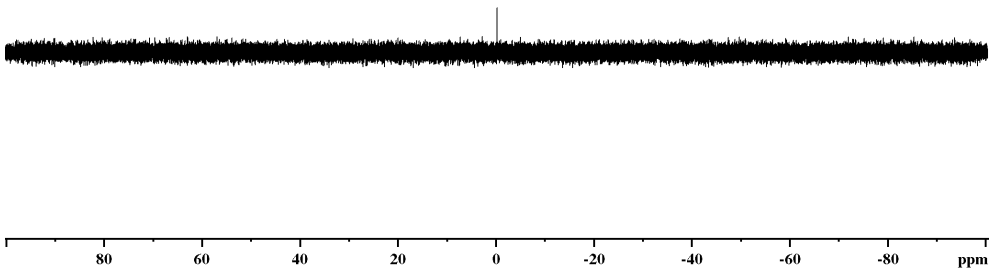

Figure S1.10. ^{7}Li-NMR spectrum (116.66 MHz, 298 K, THF/$CDCl_3$) Synthesis of [Cy5][Al(pfad)$_4$] by reaction of Li[Al(pfad)$_4$] with [Cy5][BF_4] in CH_2Cl_2 after crystallization with n-pentane, calibrated on THF. => Li^+ is absent.

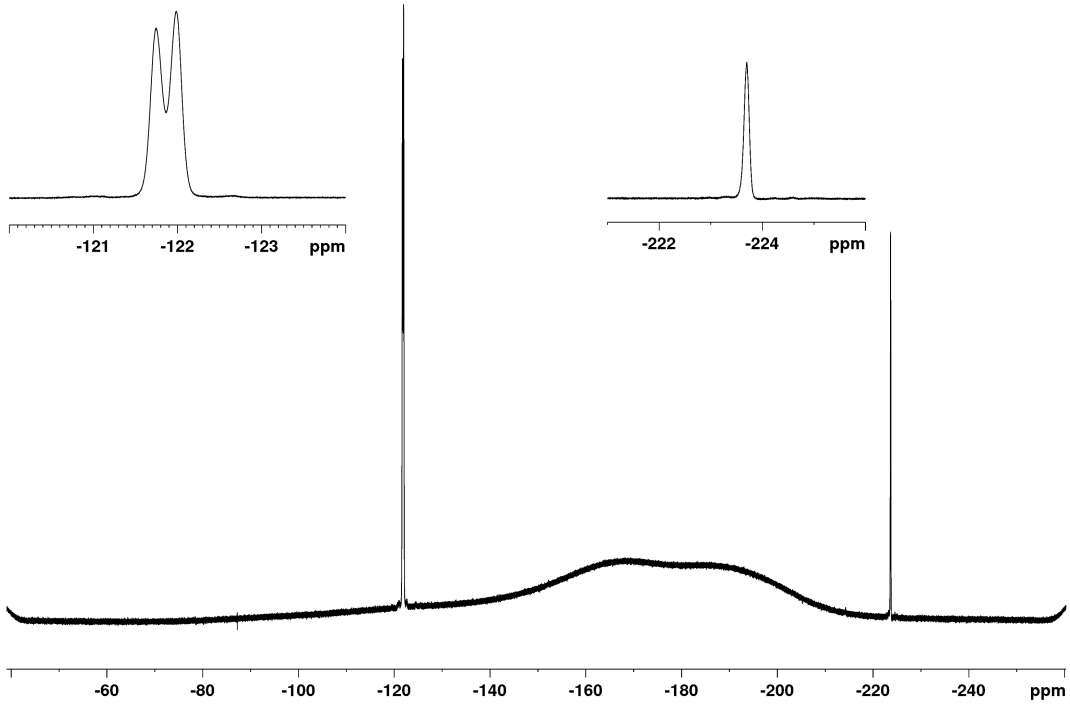

Figure S1.11. ^{19}F-NMR spectrum (282.45 MHz, 298 K, THF/$CDCl_3$) Synthesis of [Cy5][Al(pfad)$_4$] by reaction of Li[Al(pfad)$_4$] with [Cy5][BF_4] in CH_2Cl_2 after crystallization with n-pentane, calibrated on THF.

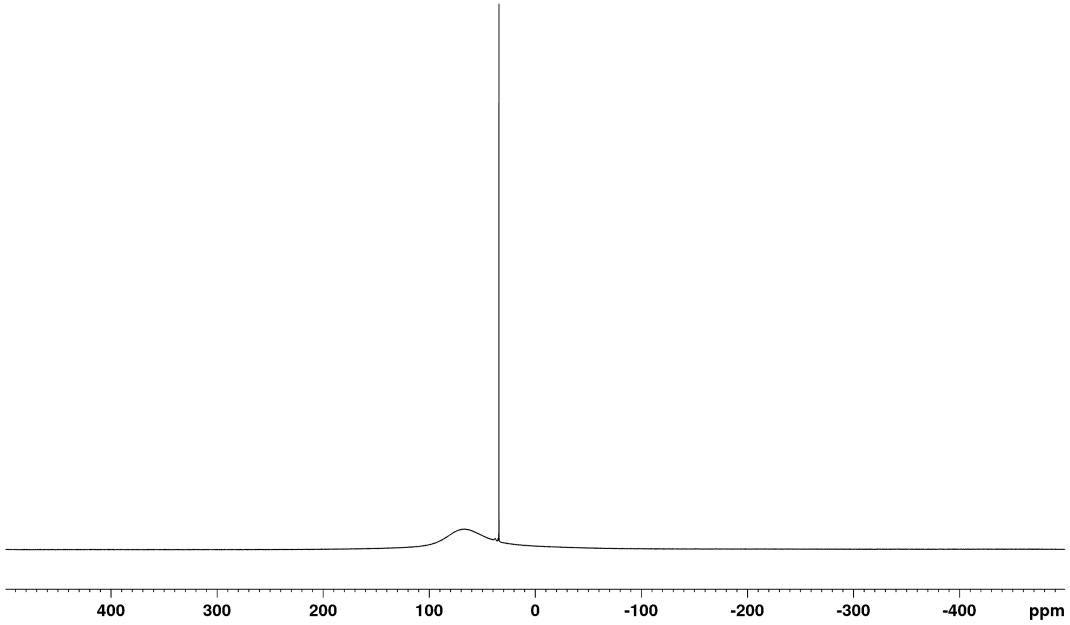

Figure S1.12. ^{27}Al-NMR spectrum (78.22 MHz, 298 K, THF/$CDCl_3$) Synthesis of [Cy5][Al(pfad)$_4$] by reaction of Li[Al(pfad)$_4$] with [Cy5][BF_4] in CH_2Cl_2 after crystallization with n-pentane, calibrated on THF.

S2. Ultrafast transient absorption dynamics and the global fitting procedure

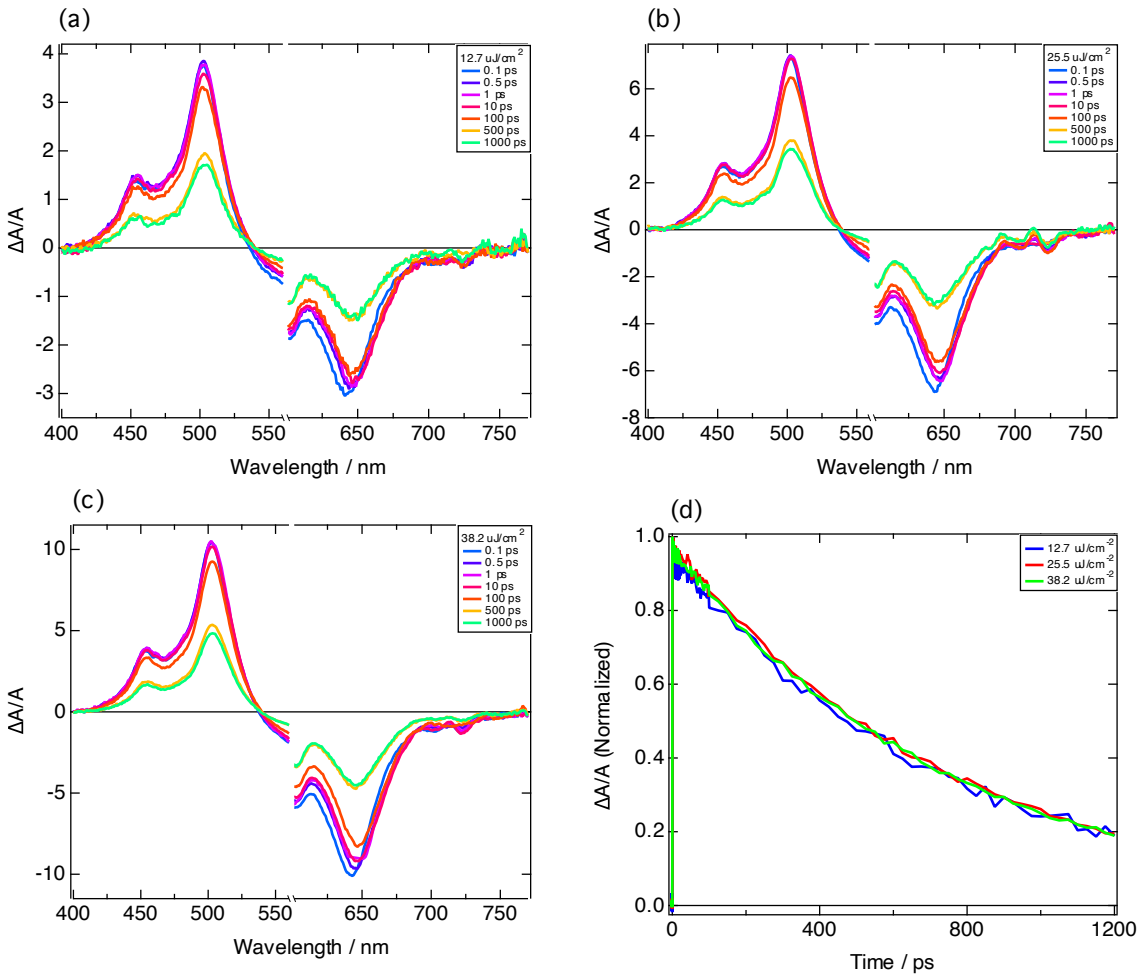

Figure S2.1. Transient absorption spectra of Cy5-P in solution at different fluences: (a) 12.7 μJcm^{-2}, (b) 25.5 μJcm^{-2} and (c) 38.8 μJcm^{-2}. Figure (d) shows the fluence independence kinetics of the feature at 502 nm.

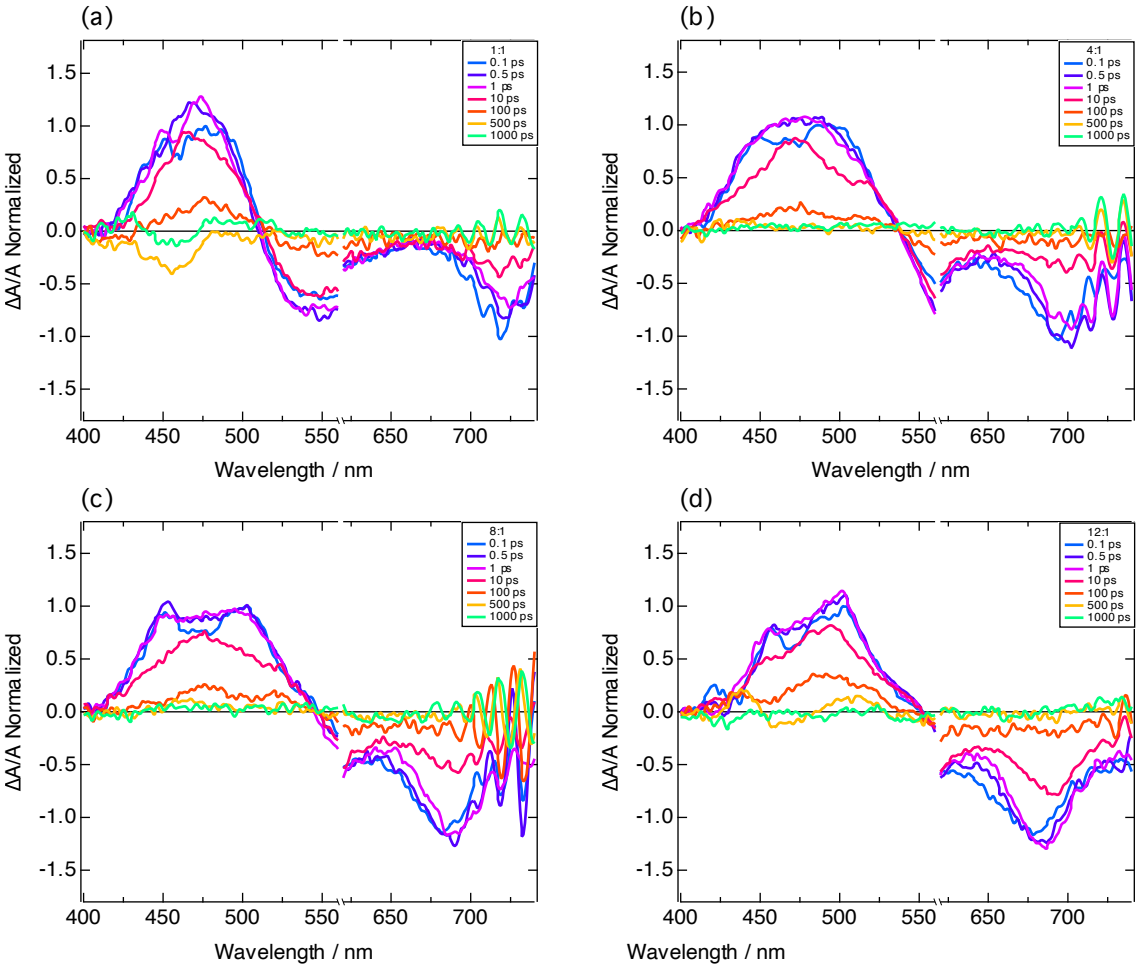

Figure S2.2. Transient absorption spectra of different PMMA:Cy5-P blends: (a) 1:1, (b) 4:1, (c) 8:1 and (d) 12:1. The spectra have been normalised to the signal at 100 fs for ease of comparison between the different blends.

Fitting of kinetic equations

The dynamic traces obtained from fs-transient absorption measurements were fitted with the following multi-exponential functions:

a) Bi-exponential function:

$$\Delta A(\lambda, t) = A_0 + A_1(\lambda) \cdot \exp\left(\frac{-t}{\tau_1}\right) + A_2(\lambda) \cdot \exp\left(\frac{-t}{\tau_2}\right)$$

b) Tri-exponential function:

$$\Delta A(\lambda, t) = A_0 + A_1(\lambda) \cdot \exp\left(\frac{-t}{\tau_1}\right) + A_2(\lambda) \cdot \exp\left(\frac{-t}{\tau_2}\right) + A_3(\lambda) \cdot \exp\left(\frac{-t}{\tau_3}\right)$$

Global Fitting Procedure [7- 9]

Global fitting was used on our data in order to help elucidate the charge transfer processes taking place within the Cy5 thin films, as well as to calculate the quantum yield of charge separation (see S5 for more details). A more comprehensive review of global analysis can be found in the following literature.[10, 11]

To perform a global fit, the data must first be sampled and an appropriate number of kinetic traces should be extracted; this allows for a suitable fit (and subsequent decay associated spectra) to be achieved, whilst minimising the amount of time required for the fit. Once sampled, a kinetic model is applied (here either a bi- or tri-exponential function) whereby all of the traces are forced to evolve with the same time constant(s). The following step-by-step procedure was used to obtain the global fits along with the use of Igor Pro (WaveMetrics) global fit software package.

1) Extract kinetics traces every 5 nm between 400 nm and 760 nm (excluding 560-620 nm due to λ_{ex} being 580 nm).
2) Manually fit a few of the extracted kinetic traces in order to obtain an accurate fitting equation and to provide a reasonable first guess for the global fit.
3) Select the appropriate fitting function from step 2. Link the time constant(s) for the kinetic traces, and provide initial values for the fitting coefficients based on the guesses found in step 2.
4) Perform the global fit with a suitable number of iterations (typically 40). If convergence is reached, assess the quality of the fit by examining the calculated residuals. If the fit does not converge, the initial guesses should be changed and the process repeated.
5) The amplitude coefficient(s) can subsequently be extracted into new sets of data, which can then be plotted against the wavelengths used in the global fit to give the decay associated spectra.

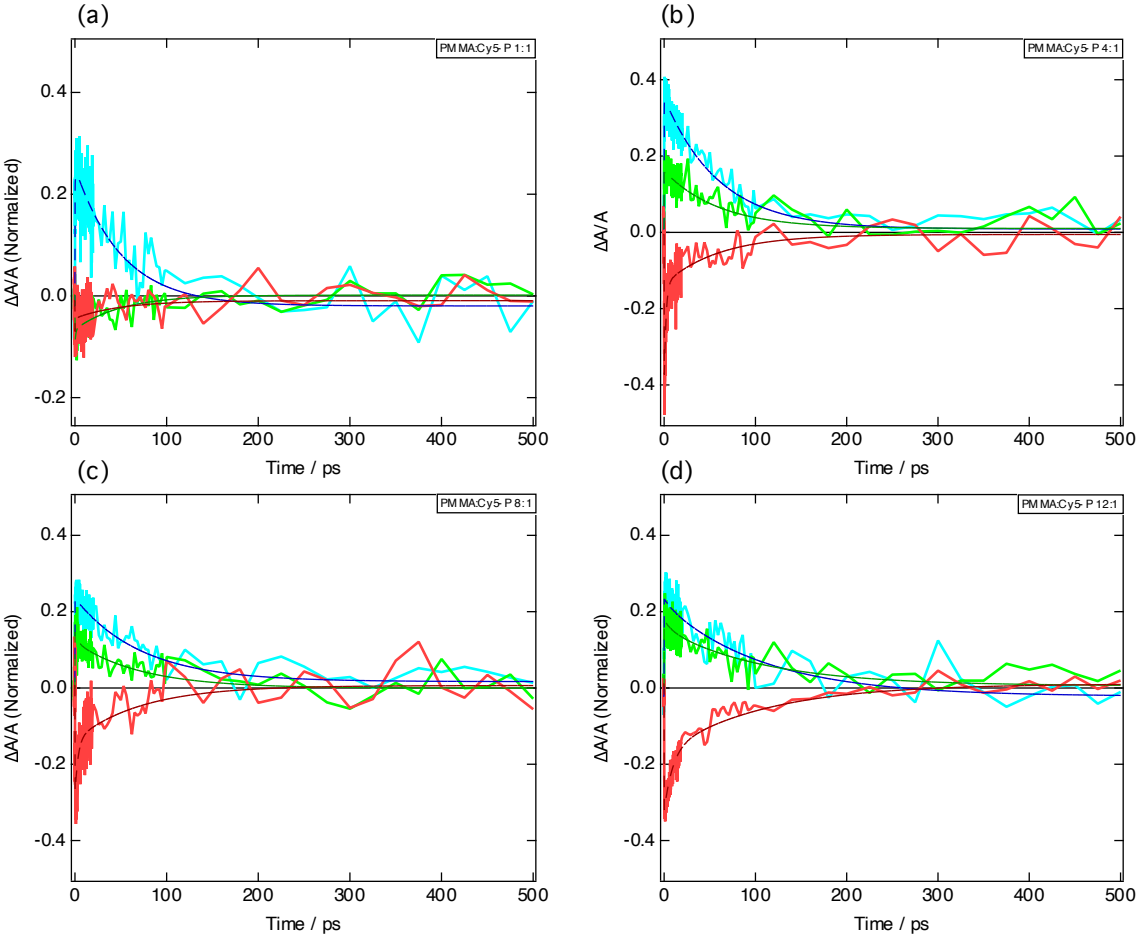

Figure S2.3. Kinetic traces at 470 (blue), 520 (green) and 700 nm (red) for different ratios of PMMA:Cy5-P thin films. The dashed lines show the results of the global fitting procedure.

Table S2. Results from global fits of TA spectra of different molar ratios of PMMA:Cy5-P blends, fitted with biexponential functions.

PMMA:Cy5-P Blend ratio	τ_1 / ps	τ_2 / ps
1:1	0.85	47
4:1	2.0	62
8:1	3.4	75
12:1	8.4	103

S3. SC-XRD details and summary of Hirshfeld surface analysis [12, 13]

Structure Tables

	Cy5-[Al(pftb)$_4$]	**Cy5-[Al(pfad)$_4$]**	**Cy5-PF$_6$**
CCDC number		2056417	2044614
Empirical formula	$C_{172}H_{124}Al_4F_{144}N_8O_{16}$	$C_{68}H_{33}AlCl_2F_{60}N_2O_4$	$C_{27}H_{31}F_6N_2P$
Formula weight	5402.70	2178.30	528.51
Temperature [K]	293(2)	100(2)	100(2)
Crystal system	monoclinic	triclinic	monoclinic
Space group (number)	$P2_1/c$ (14)	$P\overline{1}$ (2)	$P2_1/c$ (14)
a [Å]	11.4785(10)	12.925(3)	12.4822(9)
b [Å]	27.720(3)	13.451(3)	18.8248(12)
c [Å]	16.5740(16)	22.359(3)	12.0756(8)
α [°]	90	90.353(3)	90
β [°]	92.346(7)	92.653(4)	118.153(2)
γ [°]	90	93.709(4)	90
Volume [Å^3]	5269.2(9)	3874.7(12)	2501.8(3)
Z	1	2	4
ρ_{calc} [g/cm^3]	1.703	1.867	1.403
μ [mm^{-1}]	0.210	0.291	0.174
F(000)	2688	2145	1104
Crystal size [mm^3]	0.15×0.12×0.10	0.27×0.21×0.15	0.200×0.050×0.050
Crystal colour	blue	black	blue
Crystal shape	block	plate	needle
Radiation	MoK_α (λ=0.71073 Å)	MoK_α (λ=0.71073 Å)	MoK_α (λ=0.71073 Å)
2Θ range [°]	2.86 to 50.65 (0.83 Å)	1.82 to 55.87 (0.76 Å)	3.70 to 56.63 (0.75 Å)
Index ranges	-13 ≤ h ≤ 12 -33 ≤ k ≤ 32 -19 ≤ l ≤ 19	≤ h ≤ ≤ k ≤ ≤ l ≤	-16 ≤ h ≤ 16 -25 ≤ k ≤ 25 -16 ≤ l ≤ 16
Reflections collected	34148	17443	63205
Independent reflections	9269 R_{int} = 0.1611 R_{sigma} = 0.1279	17443 R_{int} = 0.0378 R_{sigma} = 0.0505	6174 R_{int} = 0.0589 R_{sigma} = 0.0331
Completeness	97.2 %	96.4 %	100.0 %
Data / Restraints / Parameters	9269/388/781	17443/18373/1968	6174/0/332
Goodness-of-fit on F^2	1.016	1.156	1.017
Final *R* indexes [I≥2σ(I)]	R_1 = 0.1165 wR_2 = 0.3021	R_1 = 0.0554 wR_2 = 0.1595	R_1 = 0.0478 wR_2 = 0.1199
Final *R* indexes [all data]	R_1 = 0.2059 wR_2 = 0.3633	R_1 = 0.0886 wR_2 = 0.1725	R_1 = 0.0690 wR_2 = 0.1344
Largest peak/hole [eÅ^3]	1.33/-0.60	0.93/-0.50	0.56/-0.42
Extinction coefficient	—	—	0.0039(7)

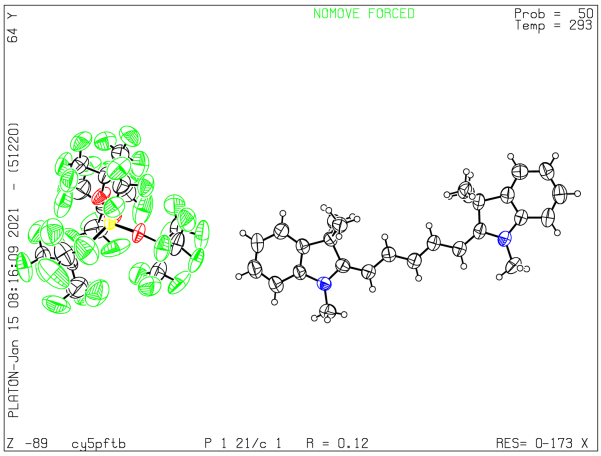

Molecular structure of Cy5-[Al(pftb)$_4$]

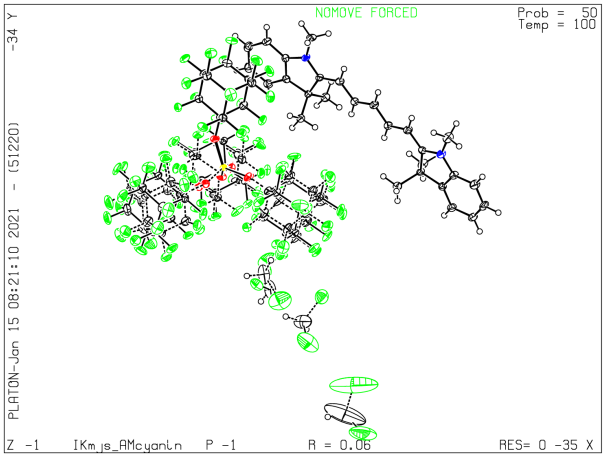

Molecular structure of Cy5-[Al(pfad)$_4$]

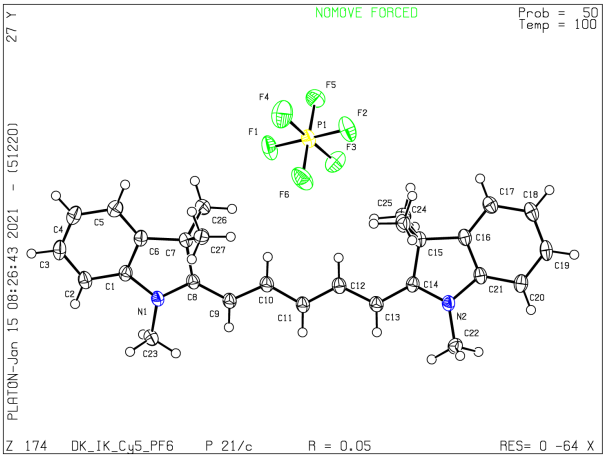

Molecular structure of Cy5-PF$_6$

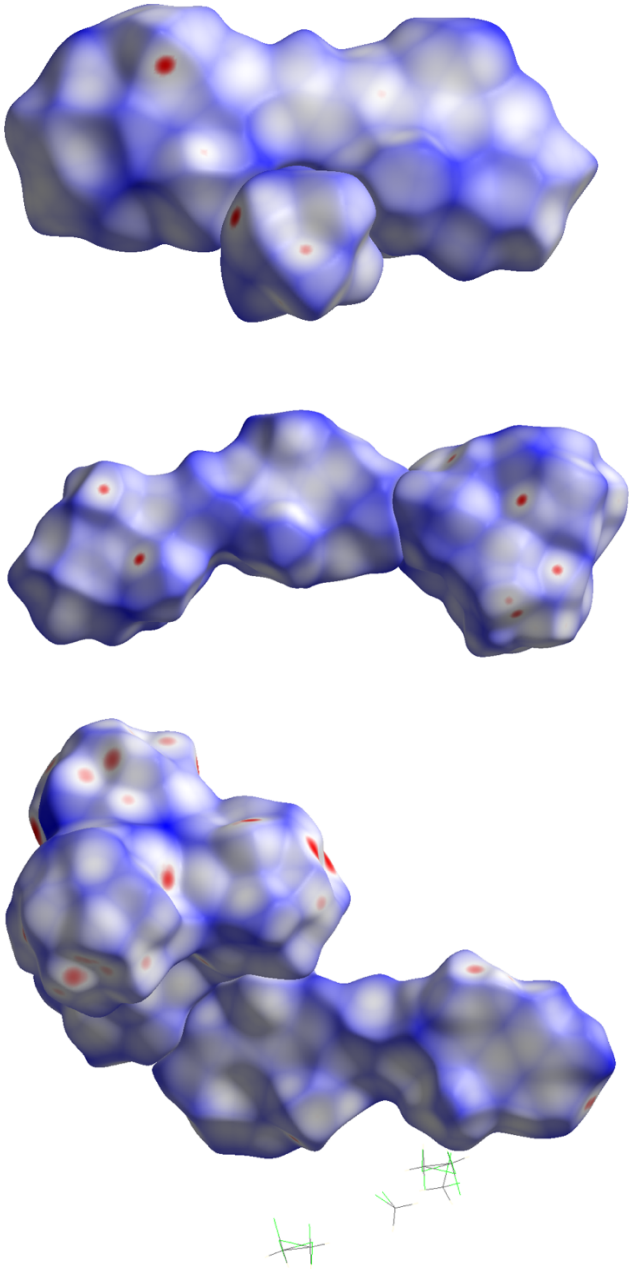

Figure S3.1. Hirshfeld surfaces of Cy5-PF_6 (top), Cy5-[Al(pftb)$_4$] (middle) and Cy5-[Al(pfad)$_4$] (bottom)

Table S3.1. Relative contributions to the Hirshfeld surface area for the intermolecular contacts in Cy5-PF6, Cy5-[Al(pftb)$_4$] and Cy5-[Al(pfad)$_4$] in percent.

	Cation					Anion		
	H...H	C...H	C...C	N...all	H...F	F...H	F...C	F...F
Cy5-PF$_6$	21.7	23.4	0.6	1.2	21.7	97.2	0.6	1.3
Cy5-[Al(pftb)$_4$]	25.6	12.7	1.0	1.0	54.3	62.2	4.0	33.5
Cy5-[Al(pfad)$_4$]	13.6	9.7	0.8	1.2	61.8	49.4	2.9	44.2

Table S3.2. Cation-Cation contacts in percent and Volume ratio of cation to anion in Cy5-PF$_6$, Cy5-[Al(pftb)$_4$] and Cy5-[Al(pfad)$_4$].

	∑Cat…Cat contacts [%]	V(C+)/V(A–)
Cy5-Cl		~18 [a)]
Cy5- PF$_6$	76.8	5.6
Cy5-[Al(pftb)$_4$]	40.5	0.8
Cy5-[Al(pfad)$_4$]	25.4	0.5

[a)] Estimated value based on V(C+) of Cy5-PF$_6$ and V(A–) of CCDC structure DODQUK.

For the cations, H-H contacts dominate for Cy5-[Al(pftb)$_4$] and Cy5-[Al(pfad)$_4$], but C-H contacts dominate for Cy5-PF$_6$. The clear difference is even more pronounced in the H-F contacts where Cy5-[Al(pftb)$_4$] has twice as many contacts as Cy5-PF$_6$ and Cy5-[Al(pfad)$_4$] even three times more. C-C and N-all contacts only play a minor role around one percent.
With the anions, there is also a clear difference for the smaller PF$_6^-$ and the other two anions. In Cy5-PF$_6$, nearly all contacts of the anion go to hydrogen atoms of the cation. But for Cy5-[Al(pftb)$_4$] and Cy5-[Al(pfad)$_4$], only 62% and 50% of the contacts are to the cation respectively. The two larger anions have more F-F contacts to other anions while PF$_6^-$ has nearly no contacts to other anions.

Cy5-[Al(pfad)$_4$]
Cation-Cation contacts: 0.8(CC)+9.7(CH)+0.9(CN)+13.6(HH)+0.4(HN) = 25,4%
Cell volume: 3874.7 Å^3
Cy5-Cation Hirshfeld volume = 573,29 Å^3
Al(pfad)$_4$ - Anion = 1194.08 Å^3

Cy5-[Al(pftb)$_4$]
Cation-Cation contacts: 1.0(CC)+ 12.7(CH)+ 1.0(CN)+ 25.6(HH)+ 0.2(HN) = 40.5%
Cell volume: 5269.10 Å^3
Cy5-Cation Hirshfeld volume = 595.12 Å^3
Al(pftb)$_4$ - Anion = 707.49 Å^3

Cy5-PF_6
Cation-Cation contacts: 0.6(CC)+0.4(NC)+0.7(NH)+23.4(CH)+51.7(HH) = 76.8%
Cell volume: 2501.8 Å^3
Cy5-Cation Hirshfeld. volume = 520,87 Å^3
PF_6 - Anion = 92.91 Å^3

Cl^-
Volume of Cl^-: ~29 Å^3

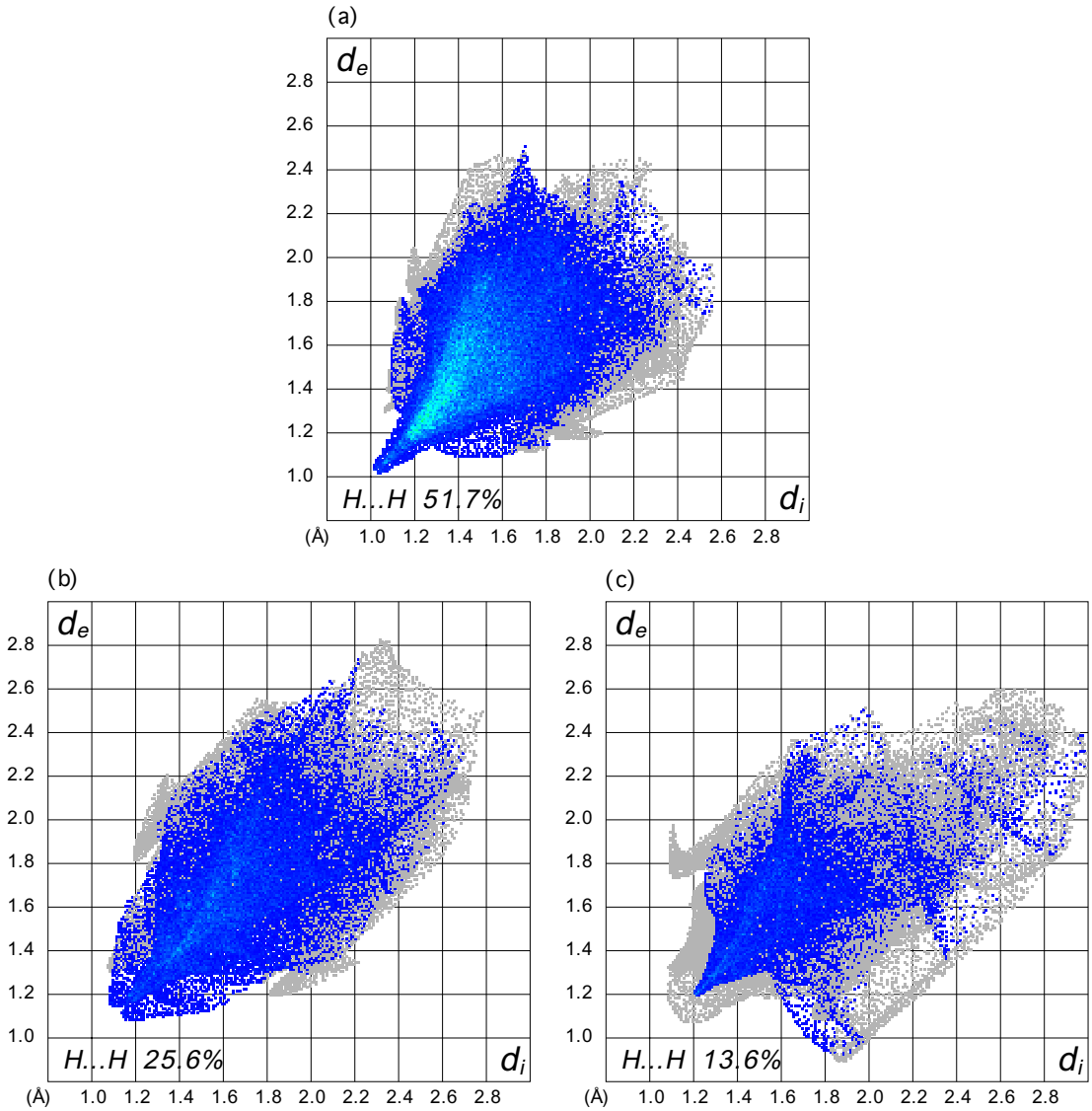

Figure S3.2. Fingerprint plots showing the distribution of inter-cationic H-H contacts for (a) Cy5-PF_6, (b) Cy5-[Al(pftb)$_4$] and (c) Cy5-[(pfad)$_4$].

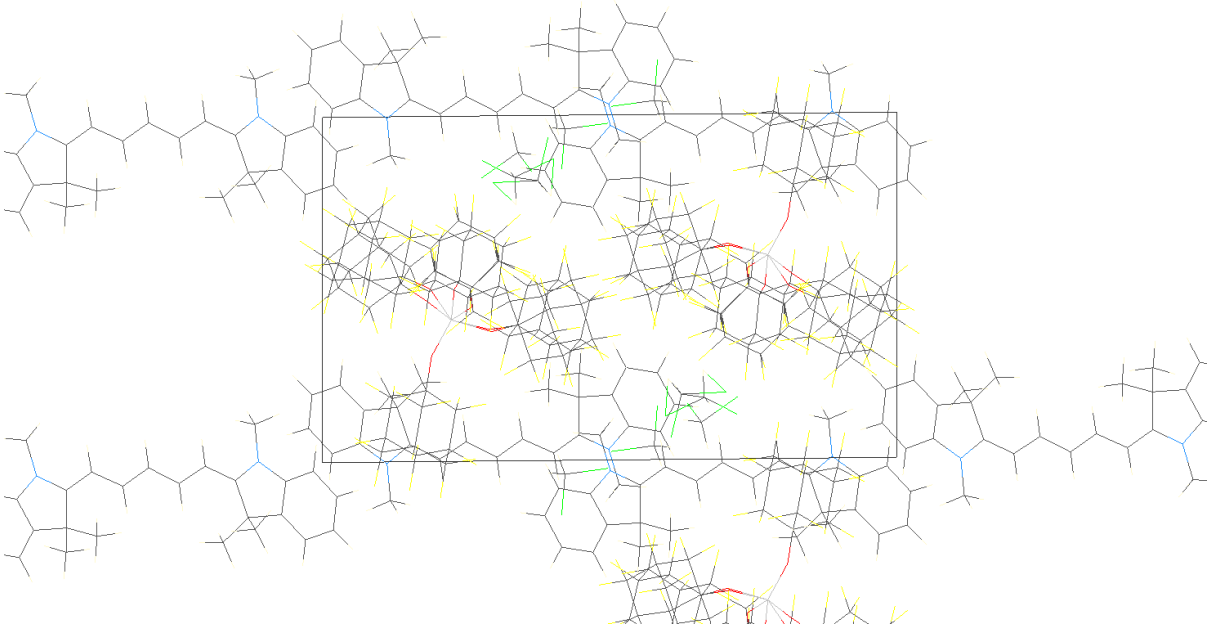

Figure S3.3. Packing of Cy5-[Al(pfad)$_4$] along a-axis.

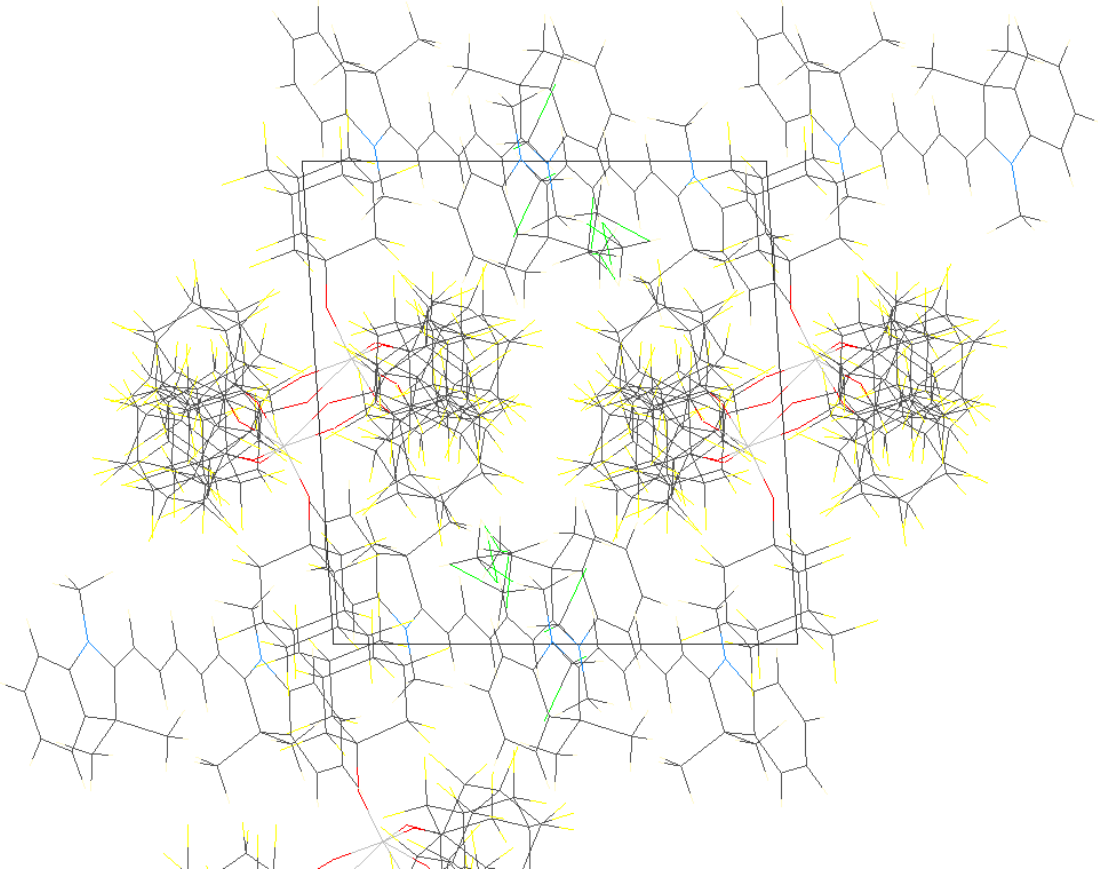

Figure S3.4. Packing of Cy5-[Al(pfad)$_4$] along c-axis.

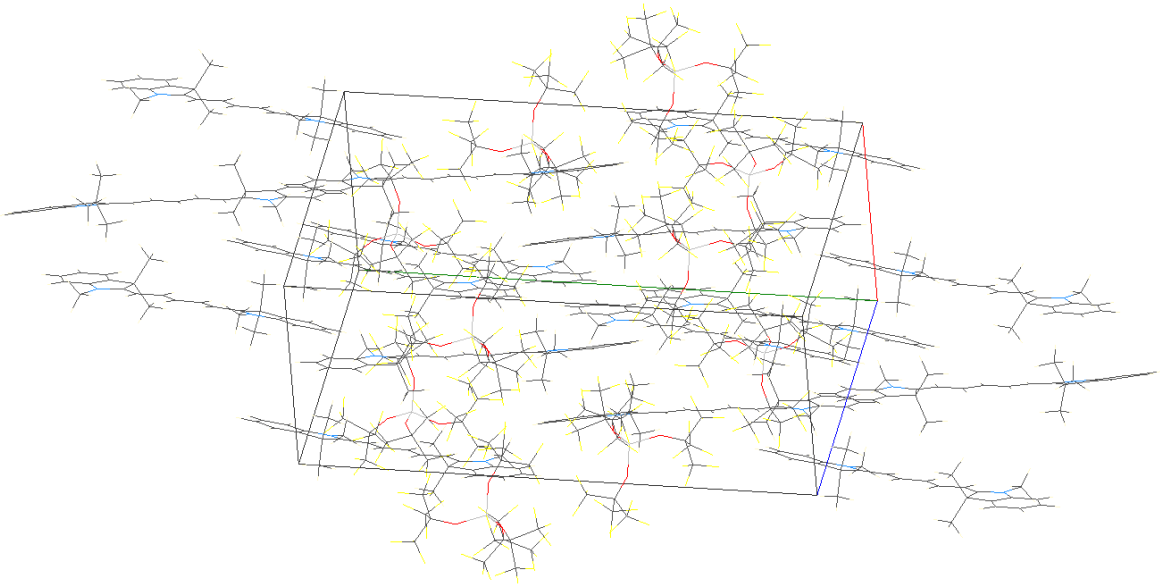

Figure S3.5. Packing of Cy5-[Al(pftb)$_4$].

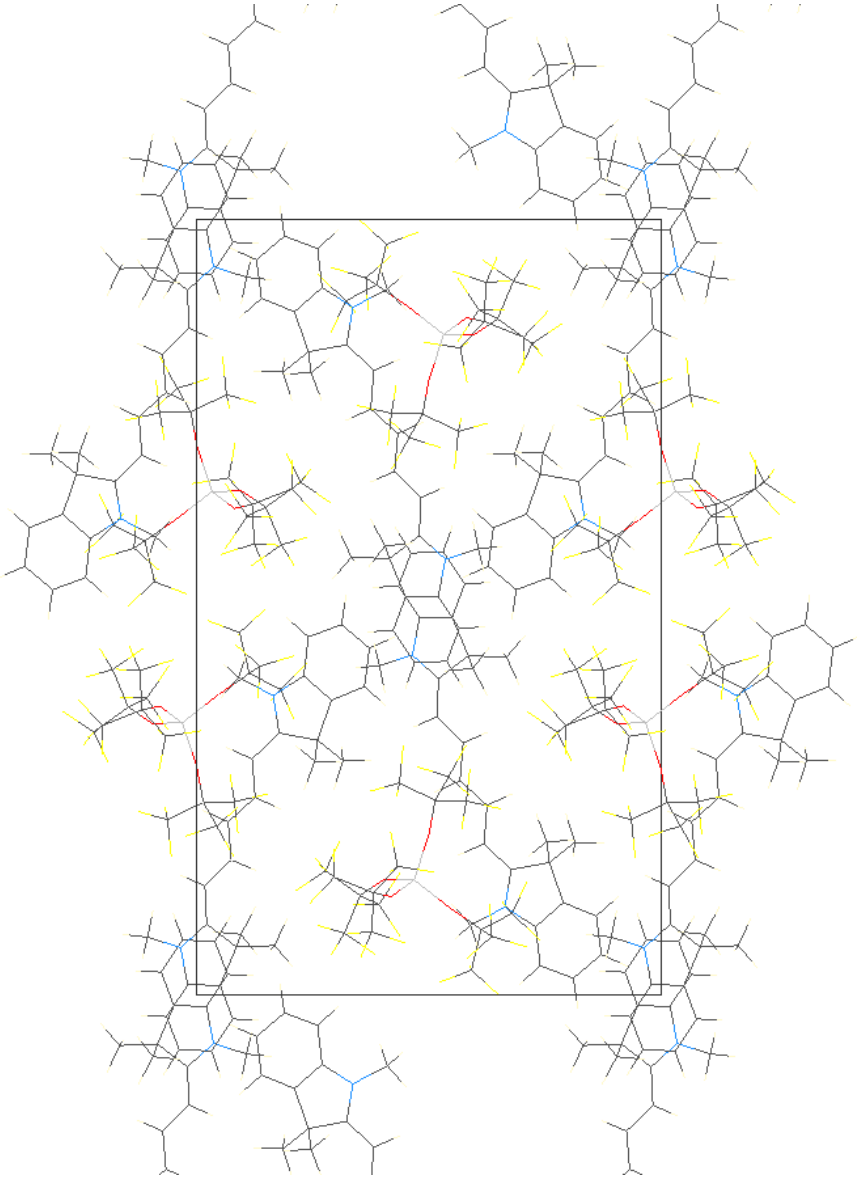

Figure S3.6. Packing of Cy5-[Al(pftb)$_4$] along a-axis.

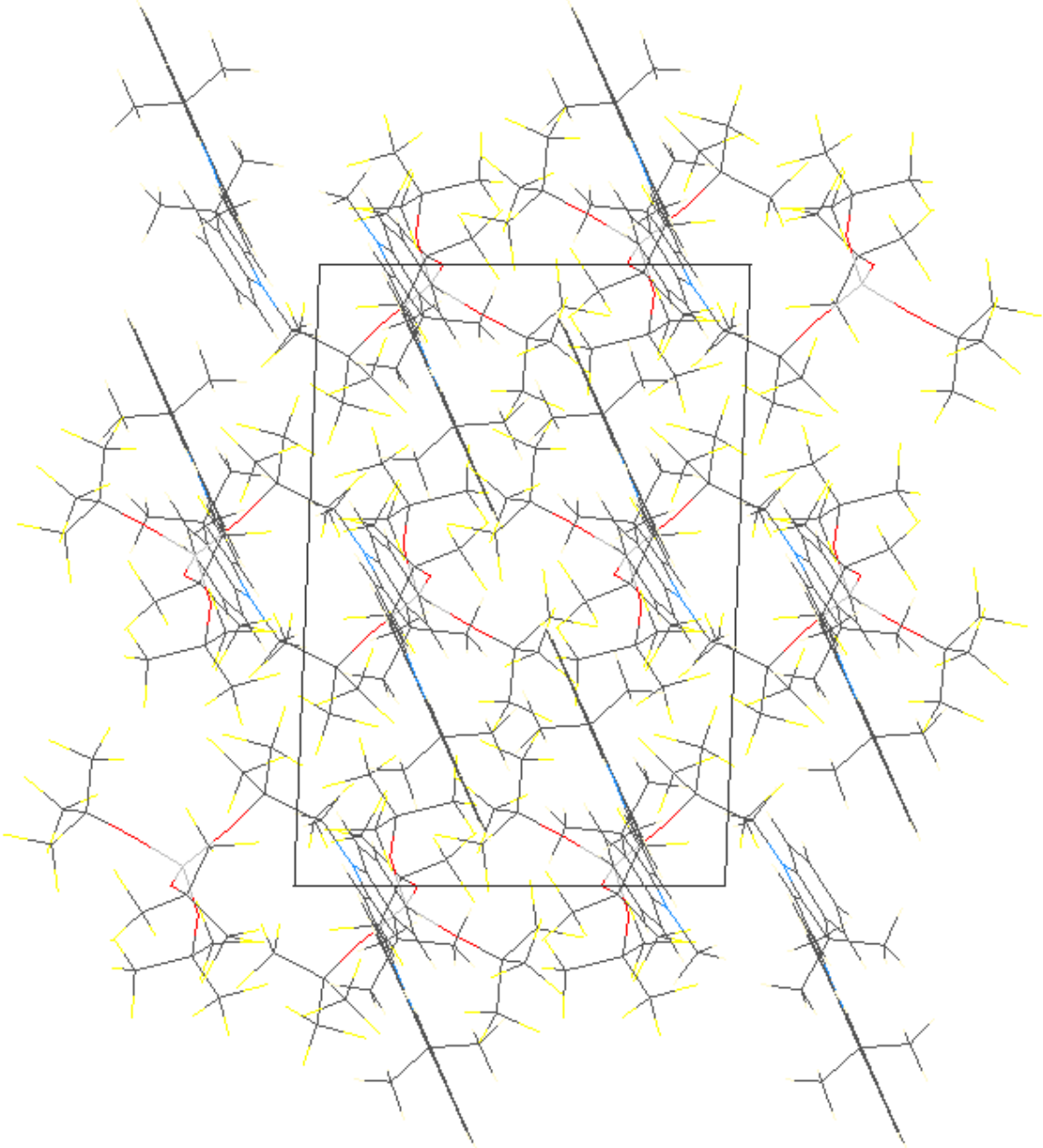

Figure S3.7. Packing of Cy5-[Al(pftb)$_4$] along b-axis.

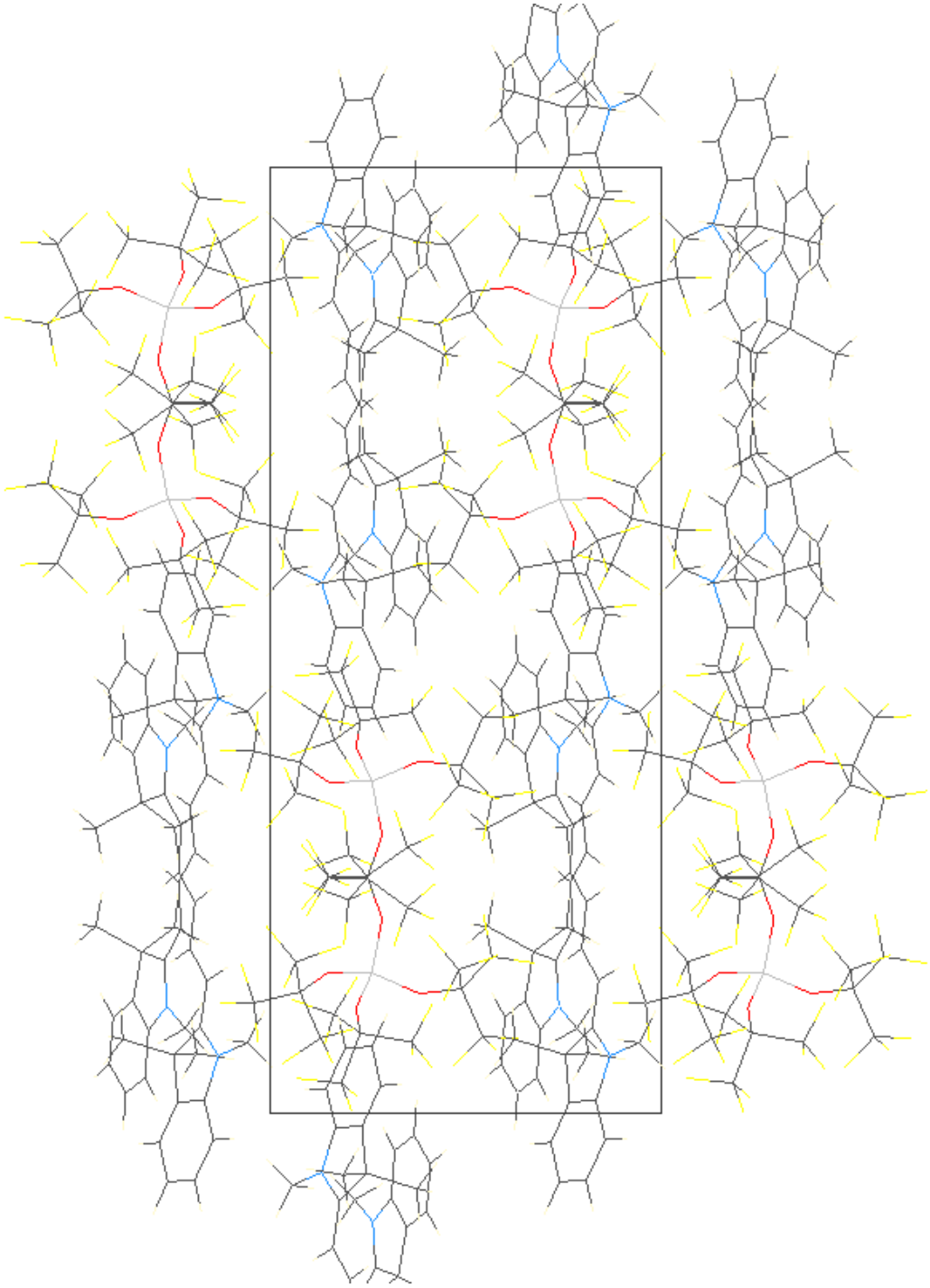

Figure S3.8. Packing of Cy5-[Al(pftb)$_4$] along c-axis.

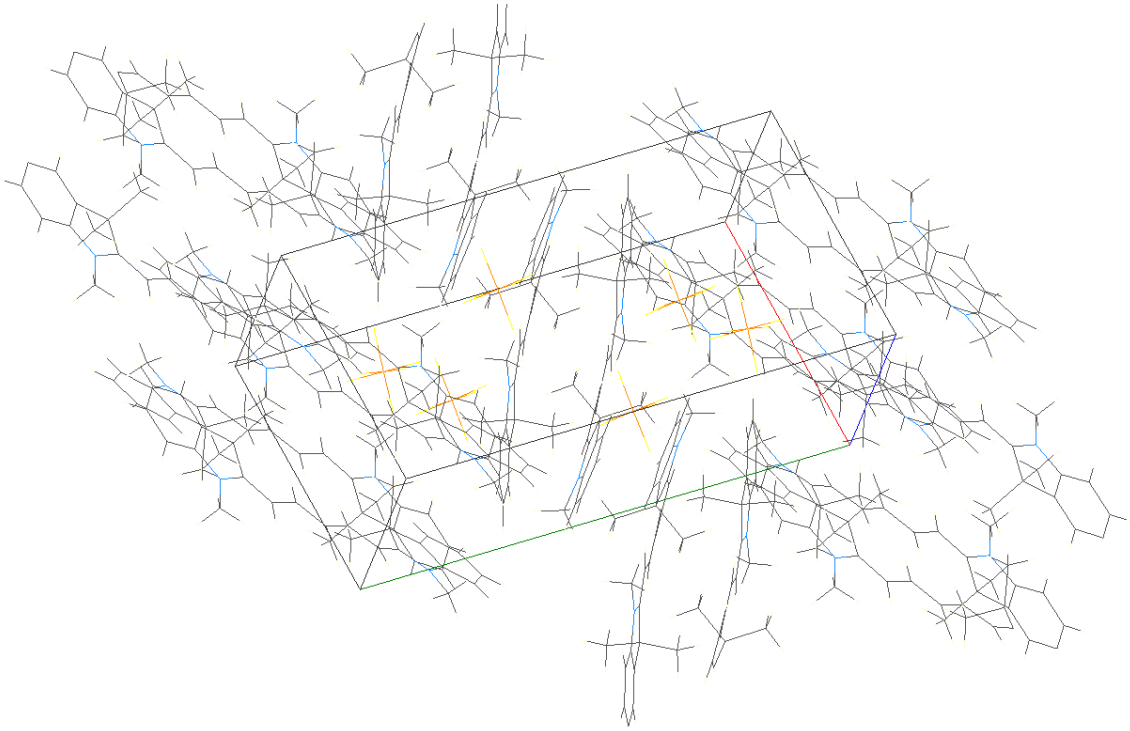

Figure S3.9. Packing of Cy5-PF_6.

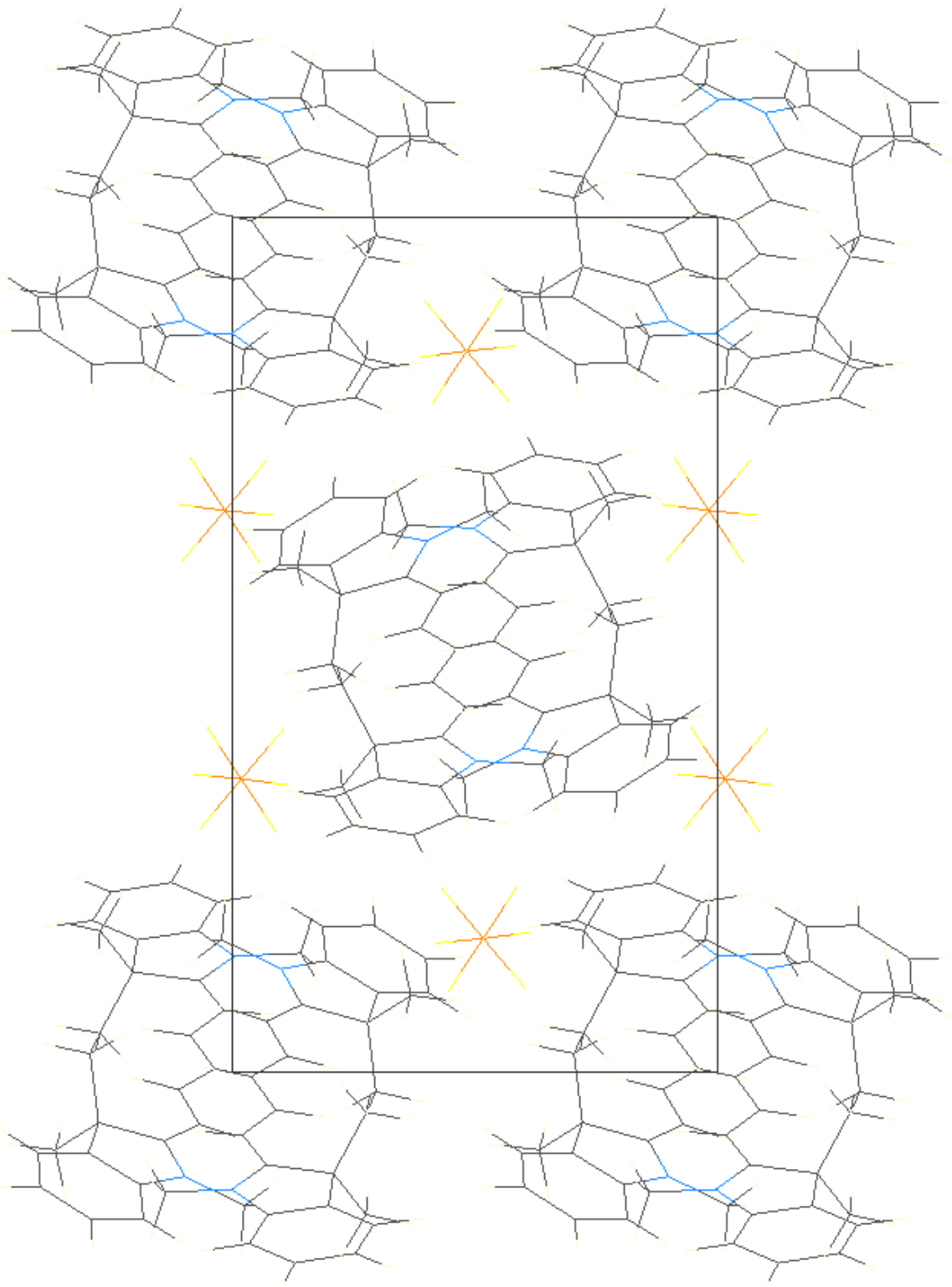

Figure S3.10. Packing of Cy5-PF_6 along a-axis.

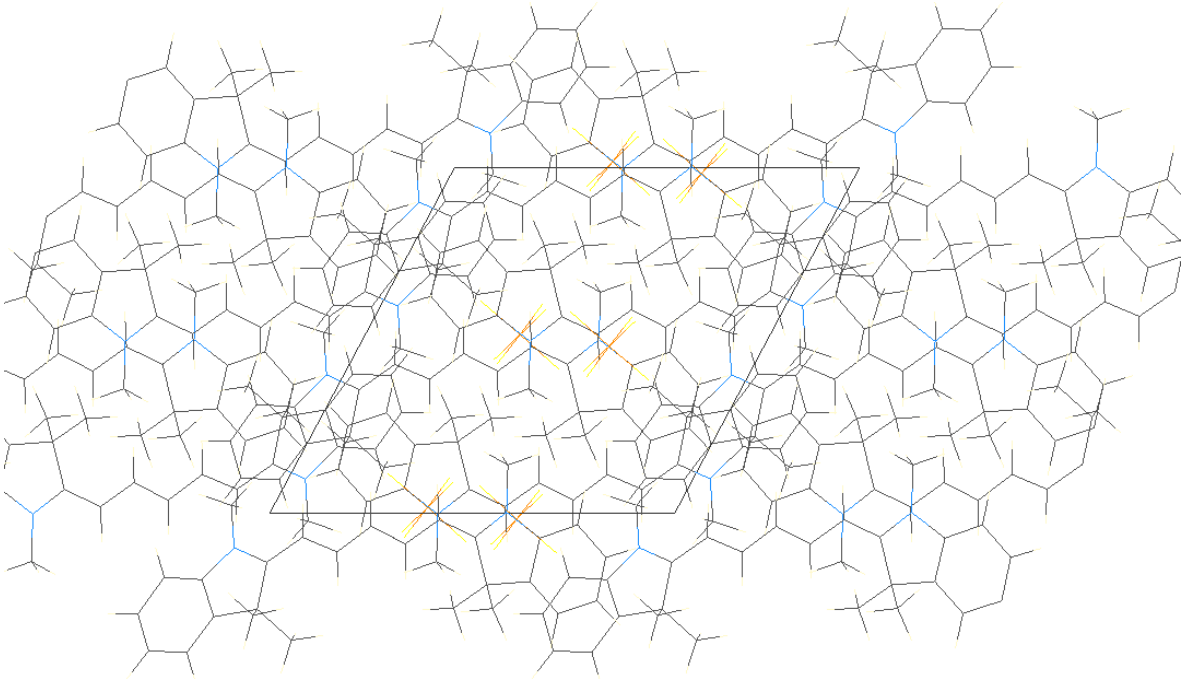

Figure S3.11. Packing of Cy5-PF_6 along b-axis

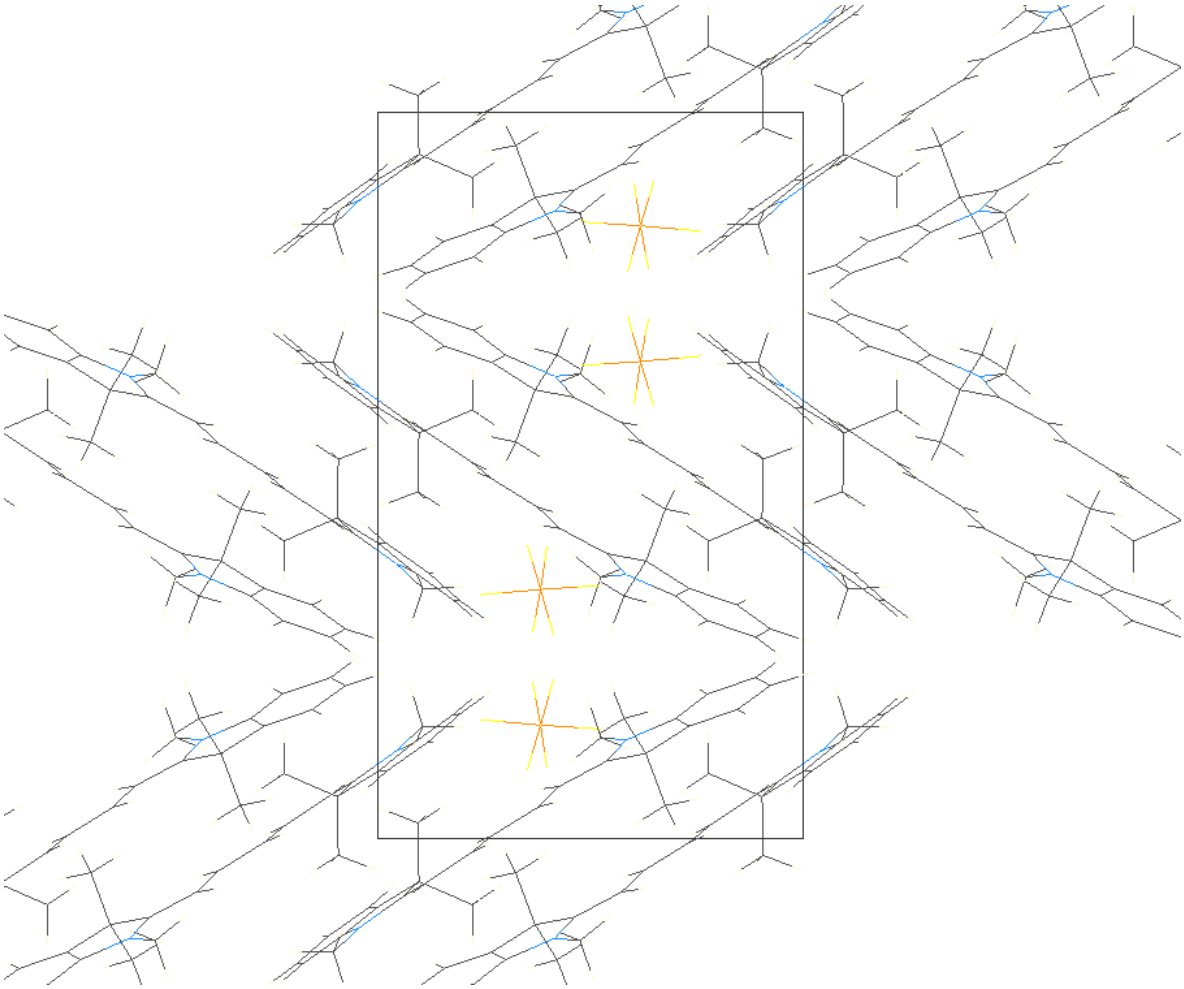

Figure S3.12. Packing of Cy5-PF_6 along c-axis.

S4. Optical characterization and global fits

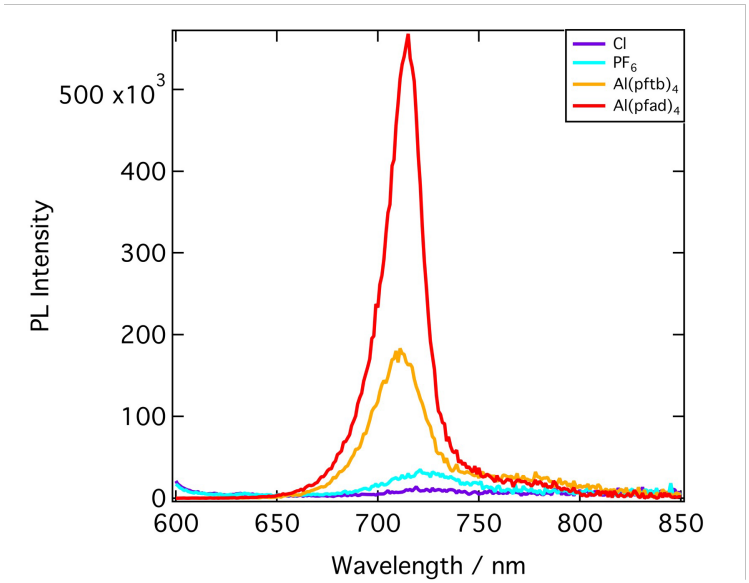

Figure S4.1. Steady state emission for different Cy5 thin films: Cl (purple), PF_6 (cyano), $[Al(pftb)_4]$ (orange) and $[Al(pfad)_4]$ (red).

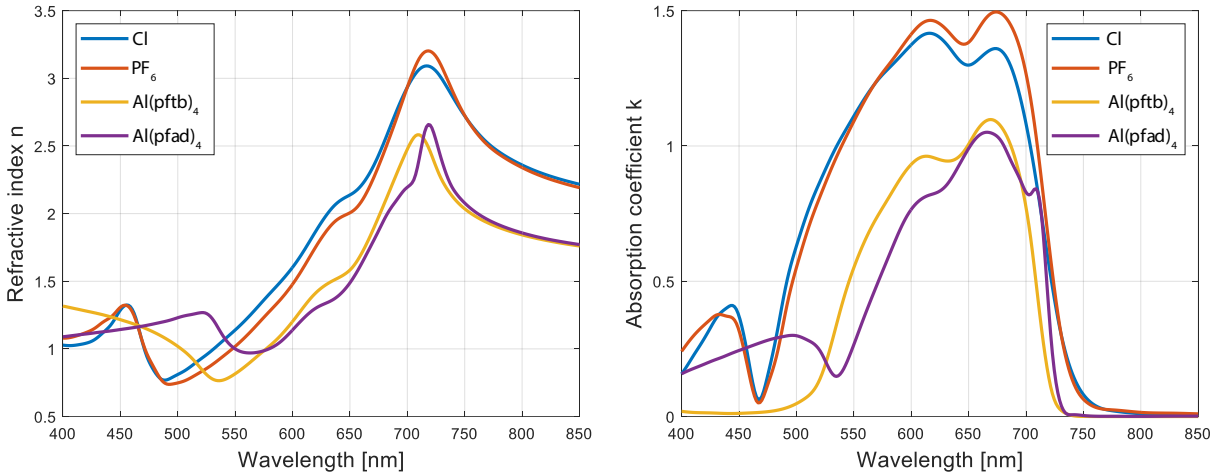

Figure S4.2. Optical constants *n* and *k* as measured by ellipsometry.

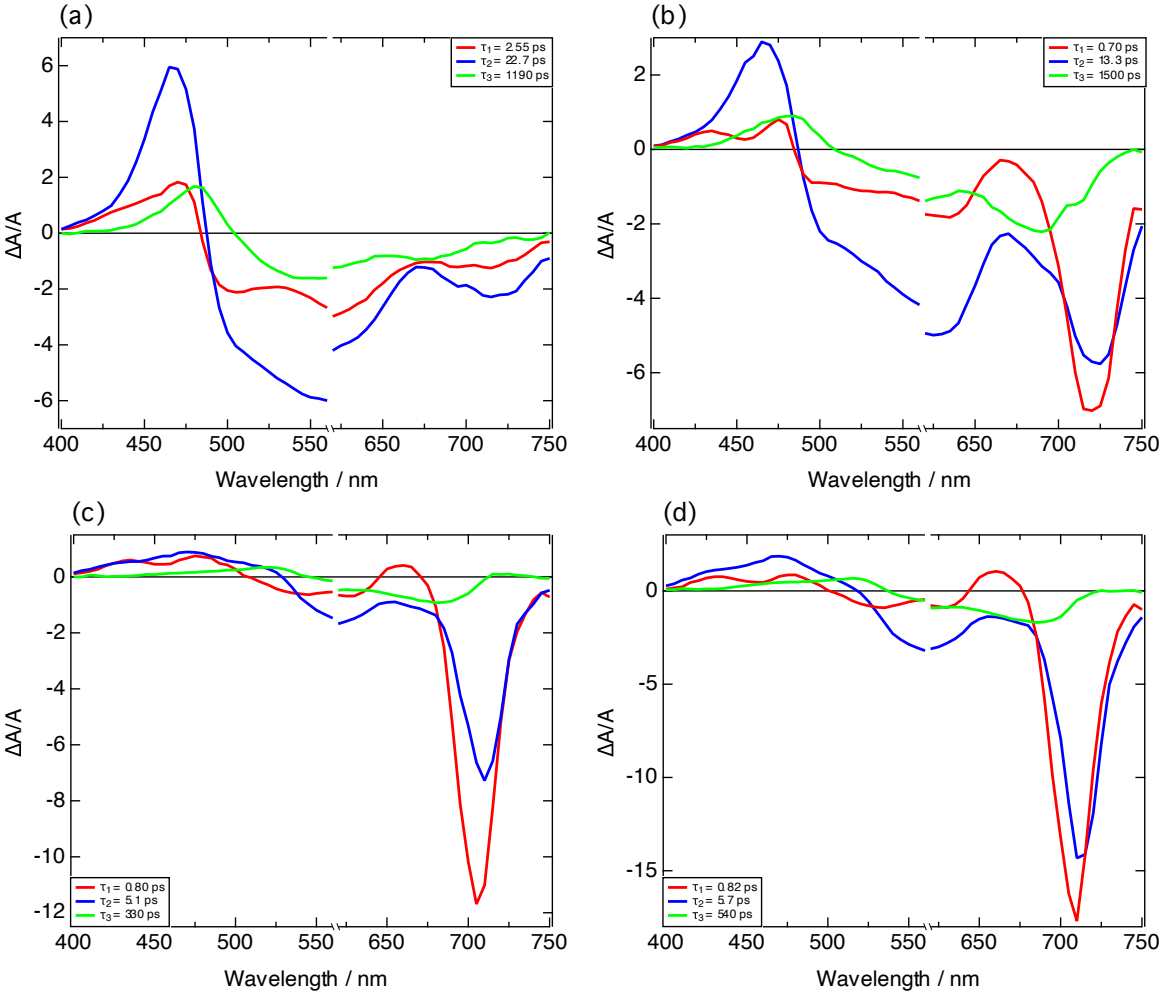

Figure S4.3. Global fits for different Cy5 thin films: (a) Cl, (b) PF_6, (c) $[Al(pftb)_4]$ and (d) $[Al(pfad)_4]$.

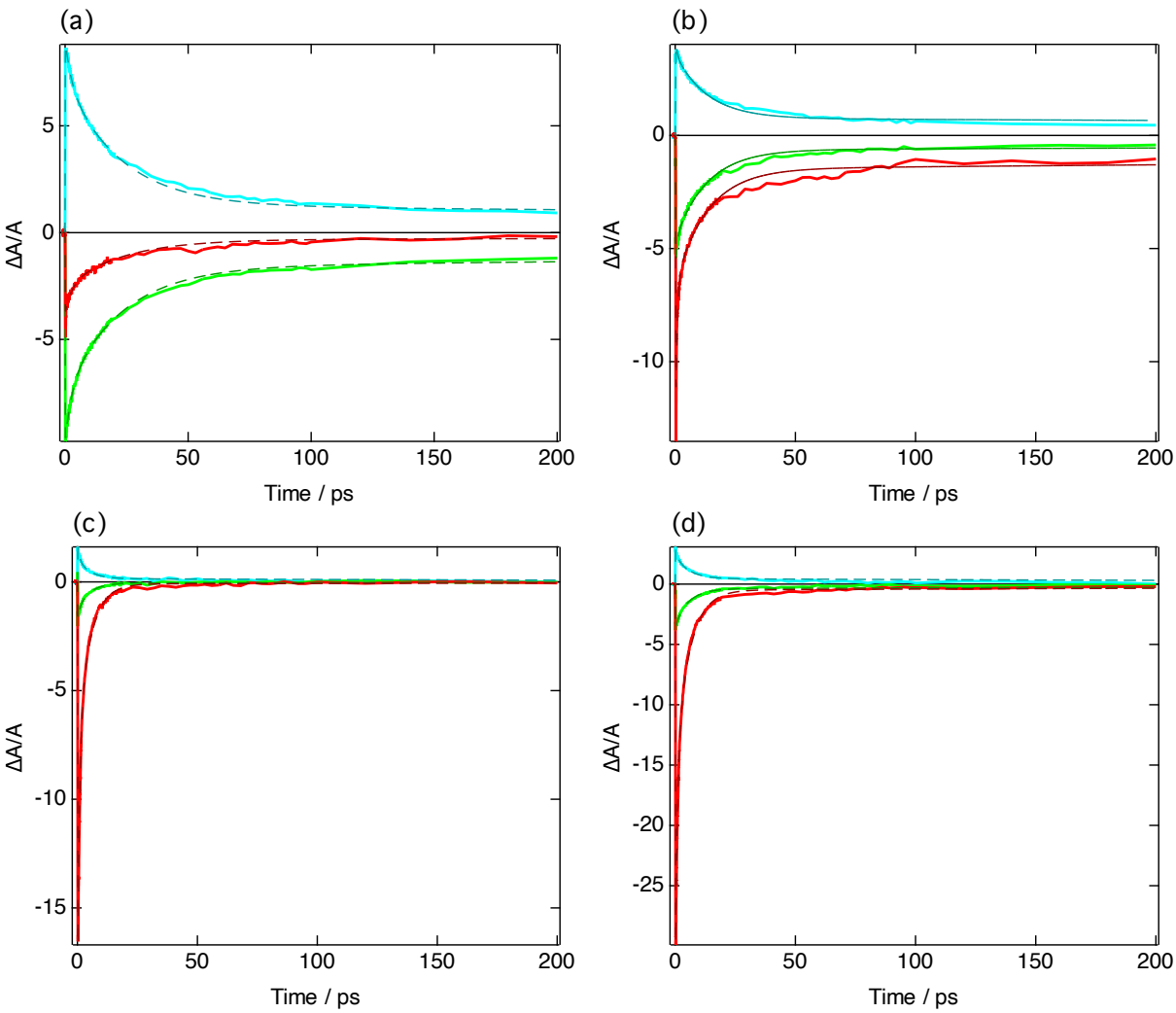

Figure S4.4. Kinetic traces at 470 (blue), 520 (green) and 700 nm (red) for Cy5-P blends incorporating different counterions: (a) Cl, (b) PF_6, (c) $[Al(pftb)_4]$ and (d) $[Al(pfad)_4]$. The dashed lines show the results of the global fitting procedure.

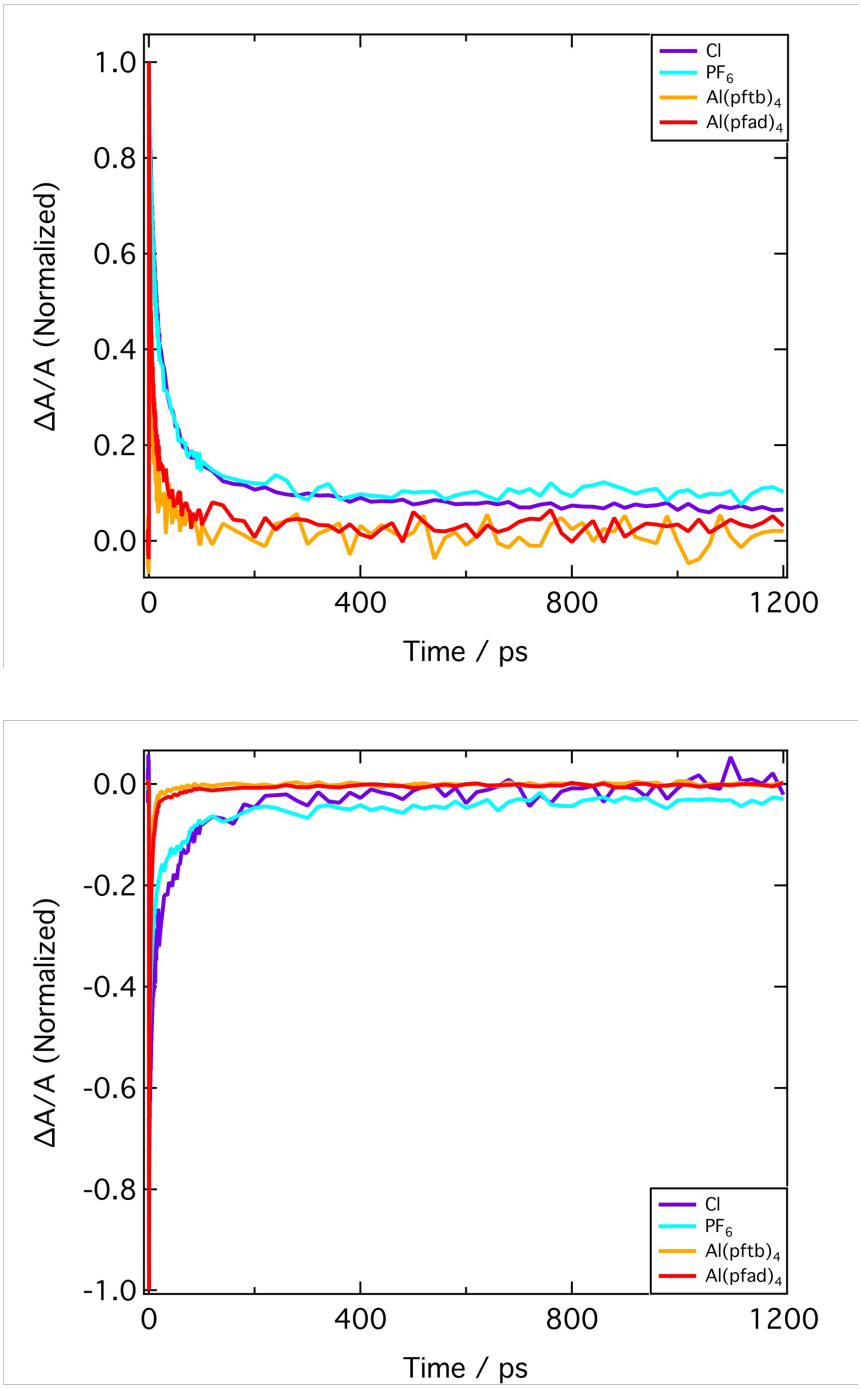

Figure S4.5. Normalized kinetic traces from TA measurements of the positive TA feature at λ = 470.5 nm (top) and the stimulated emission at λ = 710-716 nm (bottom).

S5. Estimating the quantum yield of charge separation

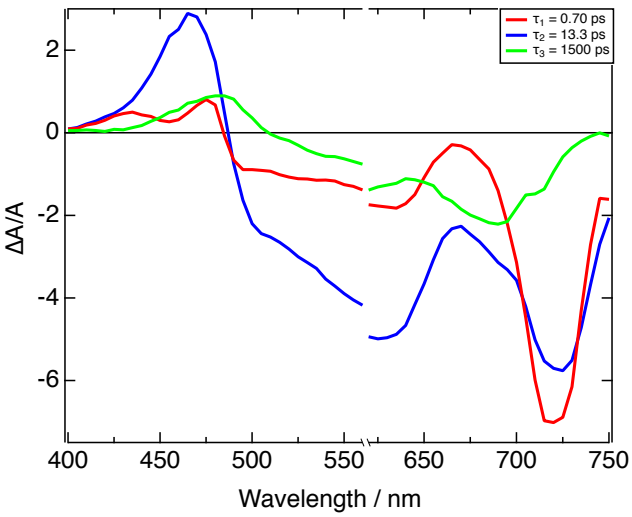

Figure S5. Decay-associated difference spectra (DADS) yielded by the global fitting of the time-evolution of transient absorption spectra.

The transient spectra were fitted with a triexponential function yielding global fit plots, an example of which is shown above for the Cy5-P thin film (Fig. S3.1).
There are three components which contribute to the TA spectrum. The first component, in red, corresponds to the appearance excited state absorption, whilst the second component, in blue, corresponds to hole transfer from the aggregate excited state to a monomer in its ground state. The third component, in green, corresponds to the recombination of the separated charges.

To estimate the charge transfer yield, the area beneath the positive feature of the curve for components A_r and A_b was found and divided by the extinction coefficients of these processes. This yields the following expression:

$$Quantum\ yield\ (\%) = \frac{A_b/\varepsilon_{ox}}{A_r/\varepsilon_{ch} + A_b/\varepsilon_{ox}}$$

Where A_r and A_b represent the area beneath the red and blue curve, and ε_{ch} and ε_{ox} are the extinction coefficients of the Cy5 chromophore and its oxidized counterpart, respectively. The extinction coefficient of the Cy5 chromophore was taken as 2.1 x 10^5 $Lmol^{-1}cm^{-1}$.

The extinction coefficient for the oxidized species was estimated from the oxidation experiments with bromine vapor, where it was found that the extinction coefficient for this process was 52 % of that of the Cy5-P dye in the ground state. Therefore, it was taken as 1.1 x 10^5 $Lmol^{-1}cm^{-1}$ for the purpose of the quantum yield calculations.

S6. Electroabsorption and time-of-flight measurements

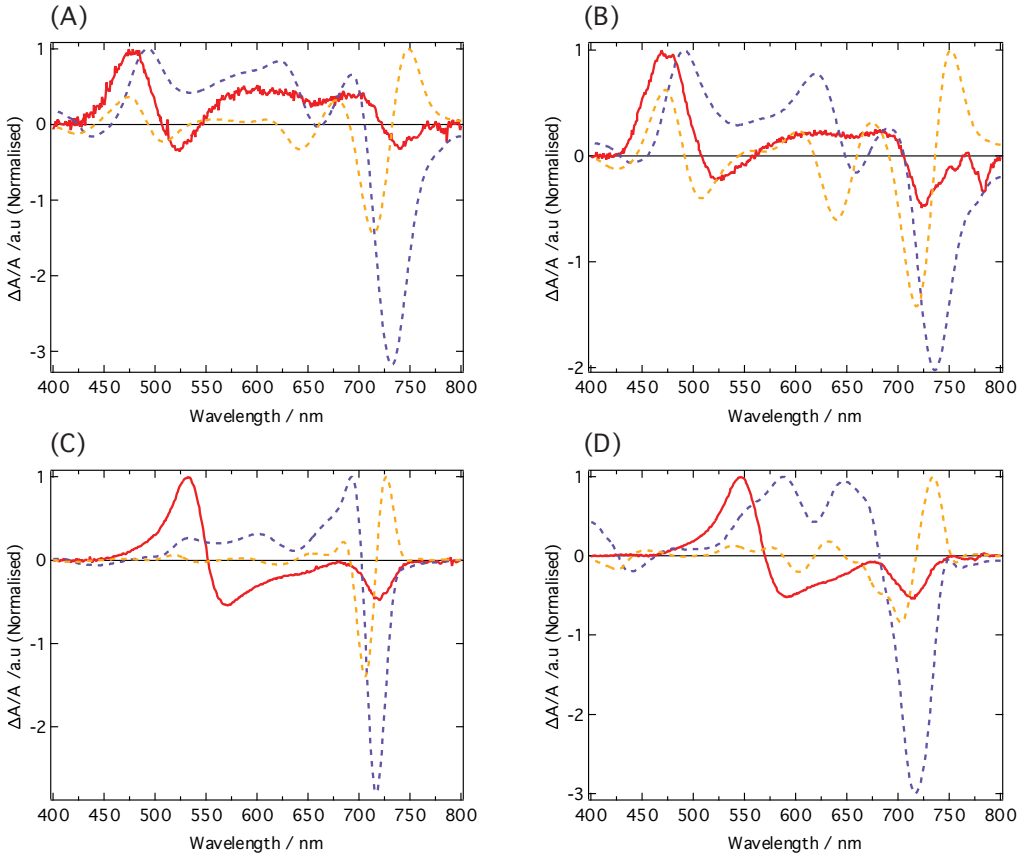

Figure S6.1. Plots showing the normalized electroabsorption spectra (red), alongside the first and second derivatives of the absorbance spectra (dashed purple and orange lines, respectively) of Cy5 dyes with various counterions: (a) Cl^-, (b) PF_6^-, (c) $[Al(pftb)_4]^-$ and (d) $[Al(pfad)_4]^-$.

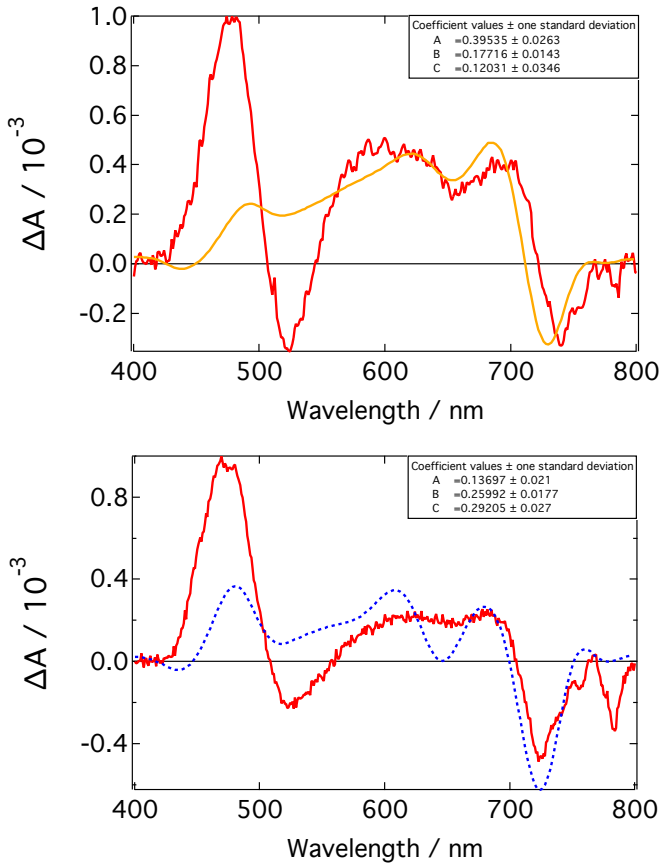

Figure S6.2. Electroabsorption spectra of Cy5-Cl (top) and Cy5-P (bottom) fitted with a linear combination of the zeroth, first and second derivatives of the steady state absorption spectra (dashed line).

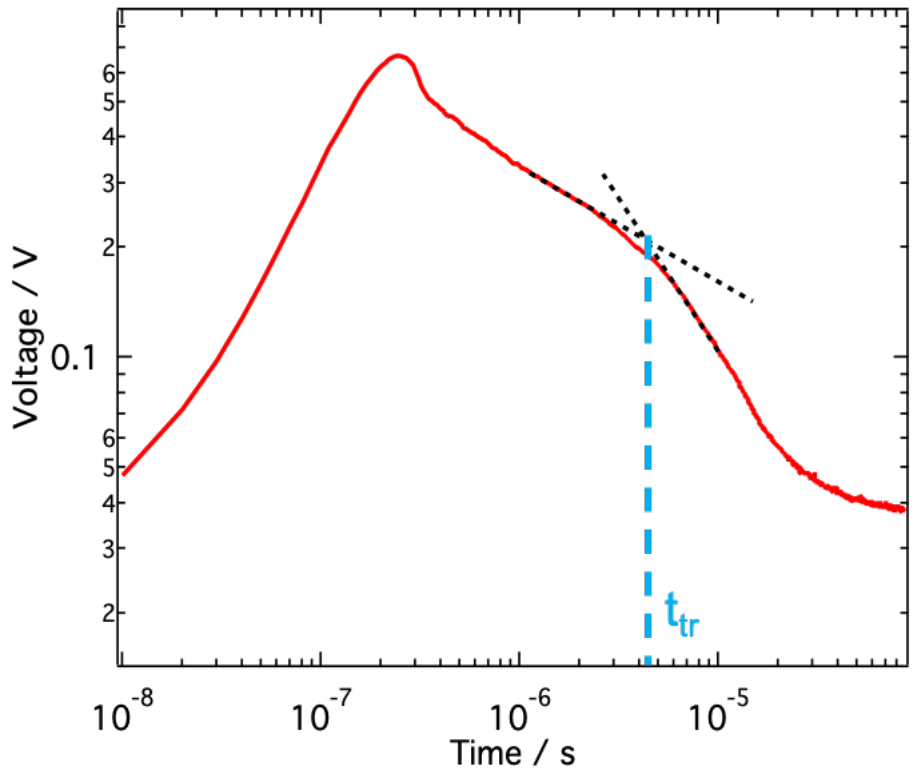

Figure S6.3. An example of a photocurrent curve from time-of-flight measurements of Cy5-P, excited at λ = 630 nm, with an applied voltage of 8 V and a resistance of 120 Ω. The transit time was found by the intersection of the two asymptotes, shown by the blue dashed line.

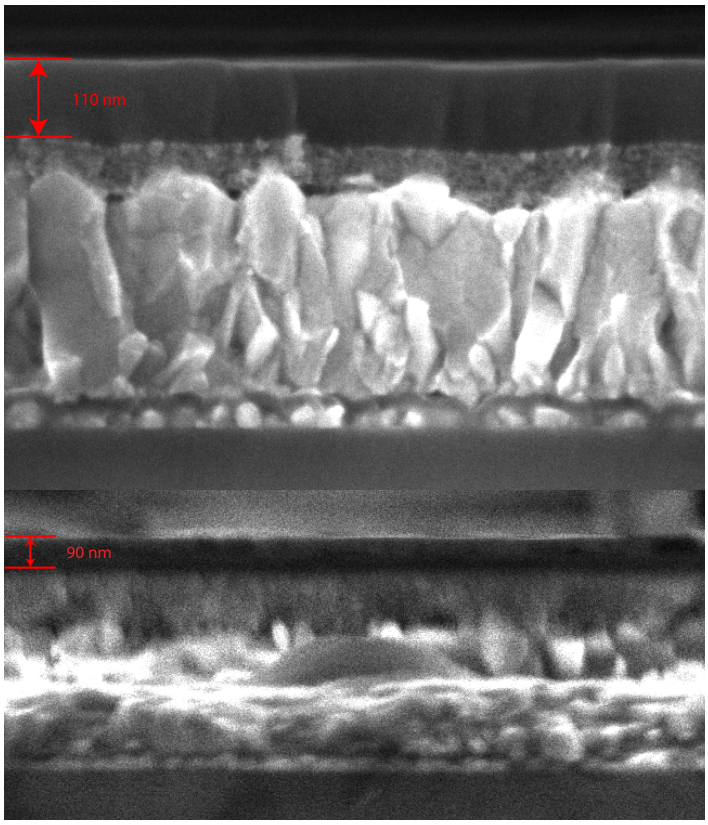

Figure S7. Cross-sectional SEM images of Cy5-Cl (top) and Cy5-P (bottom) time of flight samples. Samples had the following structure: Glass/FTO/Al_2O_3/Dye/Al. The thickness of the dye layer is shown in red.

References of SI

[1] Bruker, *SAINT*, *V8.40B*, Bruker AXS Inc., Madison, Wisconsin, USA.
[2] Bruker, *SADABS*, *2016/2:*, Bruker AXS Inc., Madison, Wisconsin, USA.
[3] G. M. Sheldrick, *Acta Cryst.*, 2015, A71, 3–8.
[4] G. M. Sheldrick, *Acta Cryst.*, 2015, C71, 3–8.
[5] C. R. Groom, I. J. Bruno, M. P. Lightfoot and S. C. Ward, *Acta Cryst.* 2016, B72, 171–179.
[6] D. Kratzert, *FinalCif*, V79, *https://www.xs3.uni-freiburg.de/research/finalcif*.
[7] M. E. F. Bouduban, A. Burgos-Caminal, R. Ossola, J. Teuscher and J. E. Moser, *Chem. Sci.*, 2017, **8**, 4371-4380 (Supporting Information).
[8] M. E. F. Bouduban, PhD thesis no. 9668, EPF Lausanne, 2019.
[9] H.-W. Bahng, PhD thesis no. 9009, EPF Lausanne, 2019.

[10] I. H. M. Van Stokkum, D. S. Larsen and R. Van Grondelle, *Biochim. Biophys. Acta-Bioenerg.*, 2004, **1657**, 82-104.
[11] R. Berera, R. Van Grondelle and J. T. M. Kennis, *Photosynth. Res.*, 2009, **101**, 105-118.
[12] N. A. Spackman and D. Jayatilaka, *CrystEngComm,* 2009, **11**, 19-32.
[13] M. J. Turner, J. J. McKinnon, S. K. Wolff, D. J. Grimwood, P. R. Spackman, D. Jayatilaka, M. A. Spackman, *CrystalExplorer17.5*, 2017, University of Western Australia.